JOURNAL OF PETROLOGY | VOLUME 47 | NUMBER 11 | PAGES 2149–2184 | 2006 | doi:10.1093/petrology/egl040

Evolution of the Lithospheric Mantle beneath the Marsabit Volcanic Field (Northern Kenya): Constraints from Textural, *P–T* and Geochemical Studies on Xenoliths

BENJAMIN KAESER[1]*, ANGELIKA KALT[1] AND THOMAS PETTKE[2]†

[1]INSTITUT DE GÉOLOGIE ET D'HYDROGÉOLOGIE, UNIVERSITÉ DE NEUCHÂTEL, RUE EMILE-ARGAND 11, CASE POSTALE 158, CH-2009 NEUCHÂTEL, SWITZERLAND

[2]ISOTOPE GEOCHEMISTRY AND MINERAL RESOURCES, DEPARTMENT OF EARTH SCIENCES, FEDERAL INSTITUTE OF TECHNOLOGY, ETH ZENTRUM NO, CH-8092 ZÜRICH, SWITZERLAND

RECEIVED NOVEMBER 18, 2005; ACCEPTED JULY 10, 2006; ADVANCE ACCESS PUBLICATION AUGUST 10, 2006

Xenoliths hosted by Quaternary basanites and alkali basalts from Marsabit (northern Kenya) represent fragments of Proterozoic lithospheric mantle thinned and chemically modified during rifting in the Mesozoic (Anza Graben) and in the Tertiary–Quaternary (Kenya rift). Four types of peridotite xenoliths were investigated to constrain the thermal and chemical evolution of the lithospheric mantle. Group I, III and IV peridotites provide evidence of a cold, highly deformed and heterogeneous upper mantle. Textures, thermobarometry and trace element characteristics of minerals indicate that low temperatures in the spinel stability field (~750–800°C at <1·5 GPa) were attained by decompression and cooling from initially high pressures and temperatures in the garnet stability field (970–1080°C at 2·3–2·9 GPa). Cooling, decompression and penetrative deformation are consistent with lithospheric thinning, probably related to the development of the Mesozoic to Paleogene Anza Graben. Re-equilibrated and recrystallized peridotite xenoliths (Group II) record heating (from ~800°C to ~1100°C). Mineral trace element signatures indicate enrichment by mafic silicate melts, parental to the Quaternary host basanites and alkali basalts. Relationships between mineral textures, P–T *conditions of equilibration, and geochemistry can be explained by metasomatism and heating of the lithosphere related to the formation of the Kenya rift, above a zone of hot upwelling mantle.*

KEY WORDS: *East African Rift System; Anza Graben;* in situ *LA-ICPMS; peridotite xenoliths; thermobarometry*

INTRODUCTION

In this study we present new data on mantle xenoliths from the East African Rift System (EARS; Fig. 1a), one of the world's largest active continental rifts. The EARS extends from the Afar triple junction in the north to Mozambique in the south. Two large-scale topographic elevations separate the EARS into two parts—the Afar dome to the north and the East African dome to the south (Fig. 1a). The boundary between them is characterized by the Turkana depression. In this zone of lower elevation, the Tertiary–Quaternary EARS transects an older (Mesozoic) rift—the Anza Graben (Fig. 1b). Mantle xenoliths investigated in this study were collected on the Marsabit shield volcano, northern Kenya, in the eastward continuation of the Turkana depression (Fig. 1b). Although the Marsabit volcano is situated on continental crust of the Pan-African Mozambique belt, and lies within the NW–SE-oriented Anza Graben, volcanic activity is related to the EARS.

Previous geophysical, structural and petrological studies have provided a fairly detailed understanding of the rifting mechanisms related to the formation of the Anza Graben and the EARS, and of the associated volcanic products. The Anza Graben is believed to represent a failed branch of a late Jurassic–early Cretaceous rift associated with the separation of Madagascar and the African continent (Reeves *et al.*,

*Corresponding author. Telephone: +41 32 718 26 80. Fax: +41 32 718 26 01. E-mail: benjamin.kaeser@unine.ch

†Present address: Institute of Geological Sciences, University of Bern, Baltzerstrasse 1, CH-3012 Bern, Switzerland.

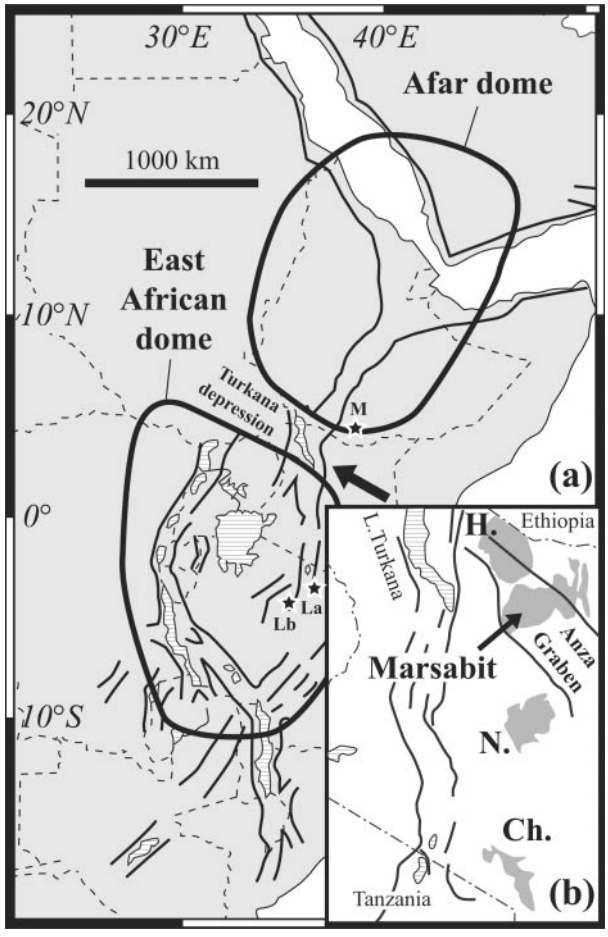

Fig. 1. Geological setting. (a) The East African Rift System, indicating the East African and the Afar domes, separated by the Turkana depression. Small stars indicate the position of other xenolith-bearing volcanic localities (M, Mega; Lb, Labait; La, Lashaine). (b) Inset shows the main structural features of the Tertiary Kenya rift (north–south) and the Jurassic–Cretaceous Anza Graben (NW–SE). Quaternary volcanic fields are shown in light grey (H, Huri Hills; N, Nyambeni; Ch, Chyulu Hills; modified from Henjes-Kunst & Altherr, 1992).

1987; Greene *et al.*, 1991; Ebinger & Ibrahim, 1993; Morley, 1999). The timing of initial rifting in the Anza Graben remains uncertain. K–Ar dating on basalts from drill holes revealed Neocomian ages (145–125 Ma; Bosworth & Morley, 1994) whereas sedimentological investigations indicate a maximum age for the onset of rifting corresponding to the Santonian (85·8–83·5 Ma; Winn *et al.*, 1993) or Neocomian (145–125 Ma; Bosworth & Morley 1994).

Tertiary volcanism in the Kenya rift (EARS-related) started in southern Ethiopia at ~45 Ma (George *et al.*, 1998) and propagated southward with time (e.g. Baker, 1987). Volcanic activity in Marsabit started in the late Miocene (7·7–5·4 Ma, Brotzu *et al.*, 1984) with the eruption of fissure-fed basalts. K–Ar dating of the Marsabit shield volcano itself has yielded ages between 0·7–1·8 Ma (Key *et al.*, 1987) and 0·5 Ma (Brotzu *et al.*, 1984). At ~2 Ma the eruption style changed from hawaiian to strombolian, leading to the formation of the mantle xenolith-bearing cinder cones and maars of alkali basaltic to basanitic composition (Volker, 1990).

A comprehensive model based on seismic refraction–wide-angle reflection experiments (Mechie *et al.*, 1997) indicates that in the south, beneath the East African dome (Fig. 1a) the crust is thick (35 km), elevation is high (2–3 km) and the rift is narrow (50–70 km wide). In contrast, in the north, beneath Lake Turkana (Fig. 1), the crust thins to 20 km, elevation decreases to about 400 m and the rift widens to 150–200 km. Increasing lithospheric thickness from north to south has also been postulated by Henjes-Kunst & Altherr (1992) on the basis of steady-state geotherms constructed from three mantle xenolith suites (<75 km beneath Marsabit, ~115 km beneath the Chyulu Hills, southern Kenya, and ≥145 km beneath Lashaine, northern Tanzania).

Numerous geophysical studies have detected low-velocity anomalies beneath various parts of the EARS, interpreted as anomalously hot upwelling mantle (e.g. Achauer & KRISP Teleseismic Working Group, 1994; Prodehl *et al.*, 1994; Fuchs *et al.*, 1997; Nyblade *et al.*, 2000; Debayle *et al.*, 2001; Weeraratne *et al.*, 2003). Whether this hot material is related to one or more mantle plumes (e.g. Ebinger & Sleep, 1998; George *et al.*, 1998) triggering lithospheric thinning in the context of active rifting, or to shallow upwelling asthensophere in the context of passive rifting (e.g. King & Ritsema, 2000), as well as the control of pre-EARS lithospheric structures (e.g. Nyblade & Brazier, 2002), is still a matter of debate. Studies of xenoliths from southern Kenya and Tanzania point to a still thick, less- or non-thinned lithosphere, comprising abundant garnet-bearing peridotite (Dawson *et al.*, 1970; Reid & Dawson, 1972; Pike *et al.*, 1980; Jones *et al.*, 1983; Henjes-Kunst & Altherr, 1992; Lee & Rudnick, 1999) that preserved pre-rift features, such as Archean Re-depletion ages (Chesley *et al.*, 1999) or Pan-African metacumulates with island arc signatures (Ulianov & Kalt, 2006). However, in some parts the deep lithosphere appears to have interacted with EARS-related, asthenosphere-derived carbonatitic and silicate melts (Cohen *et al.*, 1984; Dawson & Smith, 1988; Rudnick *et al.*, 1993; Dawson, 2002; Vauchez *et al.*, 2005). Xenoliths from the northern part of the Kenya rift, on the other hand, are dominated by spinel-bearing peridotites consistent with a thinner lithosphere (Suwa *et al.*, 1975; Henjes-Kunst & Altherr, 1992; Bedini *et al.*, 1997; Conticelli *et al.*, 1999; Rooney *et al.*, 2005; this study). Geochemical studies of Ethiopian xenoliths (Bedini *et al.*, 1997; Bedini & Bodinier, 1999; Lorand *et al.*, 2003; Reisberg *et al.*, 2004) have shown that the thinned lithospheric mantle interacted with basaltic

melts, interpreted as the products of thermo-mechanical erosion of the lithosphere above a mantle plume. Geochemical data on rift-related lavas from different localities along the EARS have been interpreted to reflect the interaction of plume-derived components with the lithospheric mantle (Class *et al.*, 1994; Stewart & Rogers, 1996; George *et al.*, 1998; Rogers *et al.*, 2000; Kabeto *et al.*, 2001; MacDonald *et al.*, 2001; Späth *et al.*, 2001; George & Rogers, 2002; Furman *et al.*, 2004).

Because Marsabit is located on the intersection of three main tectonic features, its mantle xenoliths provide a unique opportunity to put new constraints on the thermal evolution and the compositional nature of the lithospheric mantle beneath this part of East Africa. The lithosphere beneath Marsabit has a complex multi-stage evolution, probably beginning with the formation of the Mozambique belt in Proterozoic times, which includes subduction, collision and accretion events between *c.* 750 and 615 Ma (e.g. Key *et al.*, 1989; Shackleton, 1993; Stern, 1994; Meert, 2003, and references therein). These events were followed by processes related to continental rifting, first, in the context of the Anza Graben in the Mesozoic and, second, during the formation of the EARS in the Tertiary–Quaternary.

The aim of this study is, therefore, to decipher the various stages in the evolution of the lithosphere, characterized by changing P–T conditions (decompression, cooling, heating) and/or metasomatism, and, where possible, to link these stages to the geodynamic context (i.e. relation to Pan-African-, Anza-, and/or EARS-related porcesses). To this end, we have chosen a set of xenolith samples that cover the entire range of peridotite types found in the volcanic rocks from Marsabit. We combine a 'classical' petrographic–petrological approach, including classification of the mantle xenoliths, major element compositions of minerals, thermobarometry, and mineral zoning patterns, with a detailed study of trace elements in minerals.

ANALYTICAL METHODS

Major elements in minerals were analysed using a CAMECA SX 50 electron microprobe equipped with four wavelength-dispersive spectrometers (Mineralogisch-Petrographisches Institut, Universität Bern) and a CAMECA SX 51 electron microprobe with five wavelength-dispersive spectrometers (Mineralogisches Institut, Universität Heidelberg). Routine analyses were carried out using 15 kV and 20 nA operating conditions on both instruments. Counting times were 20 s for most elements. Natural and synthetic silicates and oxides were used as standards. Raw data were corrected with a routine PAP program.

Trace element contents in minerals were analysed *in situ* on polished thin sections (40–50 μm thick), using a laser ablation (LA) instrument equipped with a 193 nm ArF excimer laser (Lambda Physik, Germany) coupled to an ELAN 6100 (Perkin Elmer, Canada) quadrupole inductively coupled plasma mass spectrometer (ICPMS) at the Institut für Isotopengeologie und Mineralische Rohstoffe, ETH Zürich. The instrumental setup and capabilities have been described by Günther *et al.* (1997) and Heinrich *et al.* (2003). Operating conditions were similar to those in Pettke *et al.* (2004). Raw data were reduced using the LAMTRACE program. Laser pit sizes were between 14 and 110 μm, depending on grain size and the absence or presence of mineral, fluid or melt inclusions and of exsolution lamellae. Mineral grains were analysed in detail for major elements (electron microprobe) before LA-ICPMS analysis to obtain an internal standard for LA-ICPMS data quantification and to control intra-grain heterogeneities (e.g. zoning).

Original pyroxene and garnet compositions (prior to exsolution or decomposition, respectively) were calculated by reintegration using microprobe analyses of reaction products (orthopyroxene lamellae in exsolved clinopyroxene; spinel, orthopyroxene and clinopyroxene from symplectites for garnet). We measured at least 10 points of each phase used for reintegration to obtain statistically significant average compositions of the reaction products. Modal proportions of the phases in each reintegrated area were determined by image analysis using high-quality back-scattered electron (BSE) images. On each pyroxene grain or symplectite cluster, 3–5 areas of about 100 μm × 150 μm were reintegrated so as to be representative. In cases where exsolution lamellae were too small to be individually measured, bulk compositions were obtained by scanning [with electron microprobe (EMP)] a representative area using a defocused electron beam (~15 μm). Initial garnet compositions were calculated following the method of Morishita & Arai (2003), which uses the calculated bulk symplectite composition and subtracts the amount of an inferred 'olivine component' (from the reaction grt + ol = spl + opx + cpx) necessary to obtain a 'perfect' garnet stoichiometry. The mean olivine composition of each analysed sample was used as the 'olivine component'. The stoichiometric quality of the resulting garnet composition was then controlled by site assignment of each cation to an ideal garnet composition [$(Fe,Mn,Ni,Mg,Ca,Na)_3(Si,Ti,Al,Cr)_5O_{12}$]. Only calculated garnets satisfying stoichiometry were considered further.

Modal analyses of the whole-rocks (Table 1) were obtained by image analysis on different scales. Because of often inhomogeneous distribution of phases we used high-resolution rock slice scans to determine the amount of symplectite clusters and clinopyroxene. Spinel contents were calculated from scans of 2–3 entire thin sections from one xenolith. Initial garnet contents were obtained by redrawing the shape of symplectite clusters.

Table 1: *Mineralogy and textures of the analysed mantle xenoliths from Marsabit*

Sample no.	Group	Texture	Lithology	Modal composition (vol. %)					
				symplectites (max. initial garnet*)	ol	opx	cpx	spl†	modal metasomatism
Ke 1960/2	I	porphyroclastic	(grt)-spl-lherzolite	13·3	44	10·7	32	0·05	Ti-parg (tr.), gl
Ke 1963/1	I	porphyroclastic	(grt)-spl-lherzolite	11	50	29	10	tr.	gl
Ke 1963/2	I	porphyroclastic	(grt)-spl-lherzolite	15·5	41·1	23·2	19·2	0·05	Ti-parg (0·8 vol. %), phl (0·1 vol. %)
Ke 1965/4	I	porphyroclastic	(grt)-spl-lherzolite	19·4	41	23·9	15·7	0·05	Ti-parg (tr.)
Ke 1958/6	II	strongly recrystallized	(grt)-spl-lherzolite	9	59	25	6·6	0·5	—
Ke 1958/13	II	tabular, less recrystallized	(grt)-spl-lherzolite	9·9	58·5	20·7	10·3	0·2	gl
Ke 1958/20	II	strongly recrystallized	(grt)-spl-lherzolite	14·8	52	23·7	9·3	0·3	—
Ke 1959/24	II	strongly recrystallized	(grt)-spl-lherzolite	10·7	63·5	18·7	6·8	0·3	—
Ke 1959/25	II	less recrystallized	(grt)-spl-lherzolite	7	63·2	19·9	9	0·9	gl
Ke 781/6	III	porphyroclastic	spl-harzburgite	—	72·4	22·6	4·1	0·9	—
Ke 1959/15	III	porphyroclastic	spl-harzburgite	5	63	26	5·2	0·7	amph (0·17 vol. %), apa (tr.), gl
Ke 1965/1	III	porphyroclastic	spl-harzburgite	1·5	70·8	22·9	3·9	0·9	gr (tr.)
Ke 1965/15	III	porphyroclastic	spl-harzburgite	—	74·2	18·2	5	—	amph (0·15 vol. %), phl (tr.), gr (tr.), apa (tr.), gl
Ke 1961/1	IV	ultramylonitic	spl-harzburgite	—	87·5	10·1	1·5	0·8	—
Ke 1968/1	IV	mylonitic	spl-lherzolite	—	62	27·3	8·7	2	—

*See explanation in the Analytical Methods section.
†Excluding spinel in symplectites or clusters.
ol, olivine; opx, orthopyroxene; cpx, clinopyroxene; spl, spinel; Ti-parg, Ti-pargasite; phl, phlogopite; gl, silicate glass + microlites (cpx, ol, chromite, carbonate); amph, Ti-poor amphibole; gr, graphite; apa, apatite; tr., trace amounts.

The obtained maps were then analysed digitally. The results certainly overestimate the real initial garnet content as the size of symplectites or clusters involves both garnet and olivine consumed during the symplectite-forming reaction. These values must, therefore, be regarded as maximum garnet contents. Clinopyroxene contents were obtained by colour filtering (green for Cr-rich diopside) on rock slice scans. The accuracy of this method was tested on sample Ke 1958/20, in which the clinopyroxene content was also determined by analysis of BSE images (covering an entire thin section) as well as from thin section photomicrographs. Comparison of the results yielded deviations of less than 1% (modal clinopyroxene of 8·3% from thin section photomicrographs, 8·1% from BSE images and 8·7% from colour sampling on rock slice scans), which indicates consistency of the colour sampling method. Values for orthopyroxene and olivine were obtained by manual phase attribution on large-scale thin section photomicrographs. The obtained maps were subsequently digitized and analysed.

SAMPLE SELECTION AND MACROSCOPIC CHARACTERISTICS

The xenoliths investigated in this study were collected by Angelika Kalt and Rainer Altherr (1991 and 1992). They are hosted by basanitic and alkali basaltic scoriae and consist of peridotite, pyroxenite and other, less common, rock types such as ultramafic cumulates and gabbros. The collection of xenoliths from Marsabit comprises around 300 samples. The xenoliths have diameters from ~3 cm to 25 cm with an average size of about 10 cm. They have rounded shapes and show sharp contacts with the host lava (Fig. 2a). Most xenoliths are fresh; altered samples can be recognized by the reddish colour of the olivine grains. This study focuses on peridotite xenoliths. Sixty-six samples were investigated by optical microscopy. They were subdivided in four groups based on their mineralogy and textures: Group I (15 samples) and Group II (20 samples) are clinopyroxene-rich lherzolites and contain abundant spinel–orthopyroxene–clinopyroxene symplectites, which are interpreted as

breakdown products of former garnet [hereafter referred to as (grt)–spl-lherzolites]. The main petrographic differences are porphyroclastic textures in Group I and recrystallized fabrics in Group II. In the latter, a more or less gradual transition between the two end-members exists. Group III xenoliths (27 samples) are porphyroclastic spinel harzburgites (spl-harzburgites). Five samples of this group contain rare symplectites testifying to the former presence of garnet. The last type, Group IV (four samples) consists of spinel lherzolites and harzburgites characterized by a strongly foliated, mylonitic texture. On the basis of microscopic investigation, 15 representative xenoliths (Group I: four; Group II: five; Group III: four; Group IV: two) were selected for detailed chemical analysis (Table 1).

XENOLITH PETROGRAPHY

The textural characteristics of Group I–IV peridotites are illustrated in Fig. 2a–h. Most samples are characterized by texturally distinct generations of minerals. They are, however, not necessarily different in terms of composition. In the following discussion, first generation grains (suffix 'I') either are porphyroclasts or form a totally equilibrated texture. Second generation grains either are neoblasts in porphyroclastic samples ('IIa'), or are associated with spl–opx–cpx symplectites or clusters ('IIb').

Group I: porphyroclastic (grt)–spl-lherzolite

These coarse-grained rocks contain large porphyroclasts (~1·5–3·5 mm) of kinked olivine (ol-I), orthopyroxene (opx-I) and clinopyroxene (cpx-I) with very irregular, ragged to lobate grain boundaries (Fig. 2c). Indications of dynamic recrystallization (subgrain formation, grain boundary migration) are common. The cores of clinopyroxene porphyroclasts contain exsolution lamellae of orthopyroxene (Fig. 2c), which are, in some cases, bent, indicating that exsolution occurred before or during deformation. Clinopyroxene lamellae within opx-I are rarely observed and only very small. Exsolution in opx-I appears to be related to deformation as lamellae are typically confined and oriented normal to kink-bands. Recrystallized neoblasts (ol-IIa, opx-IIa, cpx-IIa and spl-IIa) are of smaller size (~0·25–0·50 mm) and form domains adjacent to first generation porphyroclasts. The second generation grains are characterized by a lack of exsolution lamellae and a smaller, but nevertheless observable, degree of deformation.

The former presence of garnet is indicated by very fine-grained spinel–orthopyroxene–clinopyroxene symplectites (spl-IIb, opx-IIb, cpx-IIb; Fig. 2g) forming round to ovoid aggregates. Such features are often described in mantle-derived peridotites and are interpreted to result from the garnet breakdown reaction grt + ol = opx + cpx + spl (e.g. Reid & Dawson, 1972; Wallace, 1975; Henjes-Kunst & Altherr, 1992; Morishita & Arai, 2003; Altherr *et al.*, in preparation). All Group I samples are characterized by very high clinopyroxene and garnet contents (Table 1). On hand-specimen scale, clinopyroxene and symplectites together form layers or diffuse domains, alternating with more olivine-rich domains (Fig. 2a).

Abundant Ti-pargasite and rare phlogopite indicate that there has been at least one metasomatic event. Texturally, Ti-pargasite occurs either as large grains that are in textural equilibrium with the surrounding peridotite matrix (amph-i), or associated with spl-IIb around and within symplectites (amph-ii; Fig. 2g); or as small domains replacing the rims of cpx-I and IIb (amph-iii). Large amph-i grains are sometimes associated with strongly deformed phlogopite and may contain sulfide inclusions.

Group II: recrystallized (grt)–spl-lherzolite

In contrast to Group I, the peridotite xenoliths of Group II are characterized by statically recrystallized, typically strain-free grains forming 120° triple junctions (Fig. 2d). As in Group I, spl–opx–cpx symplectites indicate the former presence of garnet. However, they are more coarse-grained and the vermicular symplectite texture is often mantled by coarse spinel and pyroxene grains (Fig. 2h). A more or less gradual transition between the porphyroclastic textures of Group I and those of Group II was observed. Less recrystallized samples still contain rare deformed porphyroclasts, whereas strongly recrystallized xenoliths show annealed textures with granuloblastic grains of equant size. Most Group II samples show a foliation defined by elongated symplectites or clusters clearly visible in rock slices (Fig. 2b). Sample Ke 1958/13 (less recrystallized) shows a weak tabular fabric. Evidence of modal metasomatism is absent, and thus this group is virtually anhydrous.

Group III: porphyroclastic spl-harzburgite

Group III xenoliths are texturally similar to Group I, but contain more olivine and less clinopyroxene. A relation to Group I is further indicated by the presence of very rare spl–opx–cpx symplectites, indicating that garnet was also present in this group. Exsolution lamellae in pyroxenes are generally absent. Group III rocks contain large holly-leaf textured spinel (spl-I; Fig. 2e), which was never observed in Group I.

In some samples, modal metasomatism has produced very complex microtextures that overprint the primary peridotite mineral assemblage. These are mainly characterized by green, Ti-poor amphibole, phlogopite, ± graphite, ± apatite, forming clusters around primary

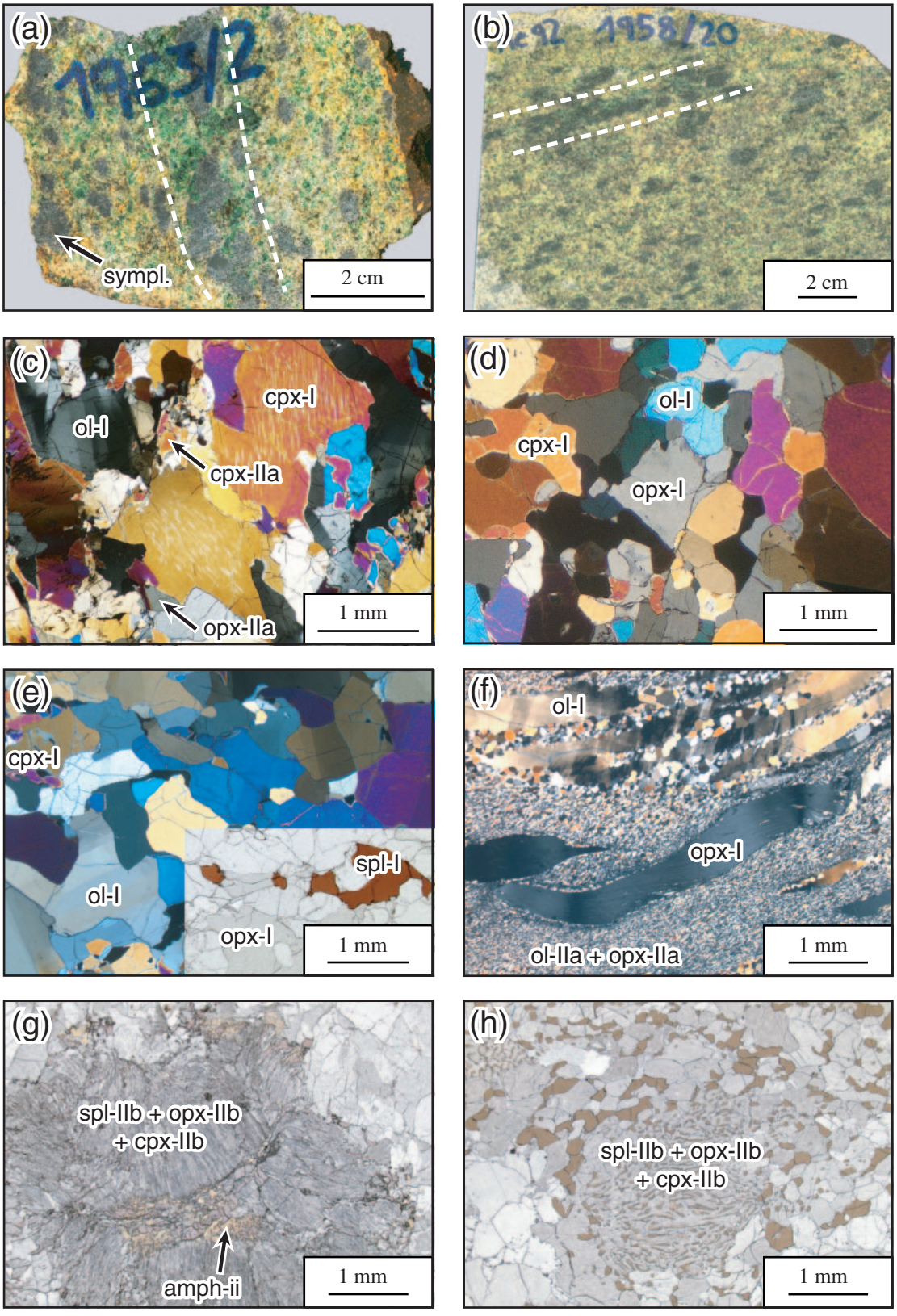
(a)
1953/2
sympl.
2 cm
(b)
1958/20
2 cm
(c)
ol-I
cpx-I
cpx-IIa
opx-IIa
1 mm
(d)
ol-I
cpx-I
opx-I
1 mm
(e)
cpx-I
spl-I
ol-I
opx-I
1 mm
(f)
ol-I
opx-I
ol-IIa + opx-IIa
1 mm
(g)
spl-IIb + opx-IIb
+ cpx-IIb
amph-ii
1 mm
(h)
spl-IIb + opx-IIb
+ cpx-IIb
1 mm

spinel or veinlets (Kaeser *et al.*, in preparation). These assemblages are then partly replaced by pockets of silicate glass associated with microlites of clinopyroxene, olivine and chromite. Compositional data for the silicate glass and the microlites indicate that their formation is not related to interaction of the xenolith with its host lava (Kaeser *et al.*, in preparation).

Group IV: mylonitic spl-harzburgite

Group IV xenoliths comprise highly deformed spl-lherzolite and -harzburgite showing a pronounced foliation (Fig. 2f). Xenolith Ke 1961/1 exhibits an ultramylonitic texture, characterized by porphyroclasts (ol-I, opx-I, cpx-I and spl-I) forming highly strained ribbons and stringers (up to ~1 cm long; Fig. 2f). In contrast, neoblasts (~0·5 –10 μm in size) are completely strain-free with perfect polygonal shapes and 120° triple junctions (Fig. 2f). Larger neoblasts are exclusively olivine, recrystallized around olivine porphyroclasts. The more fine-grained matrix consists of ol-IIa + opx-IIa (ratio about 9:1) and only very rare spl-IIa and cpx-IIa. Clinopyroxene porphyroclasts contain relatively thick orthopyroxene and spinel lamellae (>5 μm), whereas orthopyroxene clasts contain only thin (<1 μm) but very abundant clinopyroxene (+ spinel) lamellae. Exsolution probably occurred prior to the onset of deformation because the lamellae in orthopyroxene are strongly curved.

COMPOSITION OF MINERALS

Major elements

Representative compositions of olivine, orthopyroxene, clinopyroxene, spinel, amphibole, and phlogopite are given in Tables 2–5 and in a supplementary dataset available at http://www.petrology.oupjournals.org/. Results from reintegration of symplectites and exsolved pyroxenes are given in Table 6.

Olivine and spinel

Mg-numbers [$100 \times Mg/(Mg + Fe^{2+})$] of first generation olivine (Table 2) are ~89–90 in Group I and Group II xenoliths. One sample of Group II contains olivine with lower Mg-numbers (86–88; Table 2). Olivine from Group III xenoliths has Mg-numbers of ~91–92 Mg-numbers in olivine from the two Group IV samples are high in the harzburgites (Ke 1961/1; ~91–93), and somewhat lower in the lherzolites (Ke 1968/1; ~89–90). CaO contents are low in Groups I, III and IV (generally <0·05 wt %), and slightly higher in Group II (0·05–0·19; and up to 0·3 wt % in Ke 1958/6; see Table 2).

Spinel compositions are given in Table 2 and the variation with respect to Mg-number and Cr-number [$100 \times Cr/(Cr + Al + Fe^{3+})$] is illustrated in Fig. 3.

Orthopyroxene

All analysed samples contain enstatite-rich orthopyroxene with Mg-numbers ranging from ~90 to 93 (Table 3). Al_2O_3 contents are variable (Fig. 4a), mainly because of mineral zoning (see description below). The highest Al_2O_3 contents, together with relatively high CaO contents, are found in strongly recrystallized Group II samples (Fig. 4a).

Clinopyroxene

Clinopyroxenes from all samples are chromian diopsides (Table 4). The compositional variation between the groups is shown in Fig. 4b and c, showing largely negative correlations between Mg-numbers and TiO_2 contents, and between CaO and Al_2O_3 contents, with the highest Al_2O_3 and TiO_2 contents in Group II clinopyroxene (at relatively low Mg-number). In contrast, clinopyroxenes from Groups III and IV have lower Al_2O_3 and TiO_2 contents at higher Mg-number. Group I clinopyroxene is of intermediate composition. Reintegration of exsolved orthopyroxene in cpx-I from Group I slightly decreases Ca contents and Mg-number (Table 6; Fig. 4b and c).

Amphibole and phlogopite

Amphiboles from Group I xenoliths are Ti-pargasites (Table 5) with TiO_2 contents of 1·52–3·68 wt %. Mg-numbers (88·3–90·2) are similar to those of first generation olivine and orthopyroxene. Large amph-i grains are enriched in K_2O (0·74–1·34 wt %), whereas amph-ii and -iii has lower K_2O contents. Group I phlogopite composition is typical for upper mantle micas (e.g. Delaney *et al.*, 1980; Ionov *et al.*, 1997) with an Mg-number of ~90·9, high Al_2O_3, TiO_2 and Cr_2O_3, as well as considerable Na_2O contents (0·81–0·95 wt %; Table 5).

Fig. 2. Photographs (a, b) and photomicrographs (c–h) of peridotite xenoliths from Marsabit: (a) rock slice of Group I (grt)–spl-lherzolite [Ke 1963/2; note heterogeneous distribution of symplectite (grey) and clinopyroxene (dark green)]; dashed lines denote diffuse layering parallel to the foliation indicated by the ovoid shape of the symplectites; (b) rock slice of Group II recrystallized (grt)–spl-lherzolite (Ke 1958/20; dashed lines indicate layering parallel to the foliation); (c) Group I porphyroclastic (grt)–spl-lherzolite (Ke 1963/2; note orthopyroxene exsolution lamellae in cpx-I); (d) Group II strongly recrystallized (grt)–spl-lherzolite (Ke 1958/20; note strain-free grains); (e) Group III porphyroclastic spl-harzburgite (Ke 1965/1); (f) Group IV ultramylonitic spl-harzburgite (Ke 1961/1); (g) fine-grained symplectite with associated Ti-pargasite (amph-ii) in Group I (grt)–spl-lherzolite (Ke 1963/2); (h) coarser-grained symplectite in Group II (grt)-spl-lherzolite (Ke 1958/20; note coarse-grained clusters mantling symplectite).

Table 2: Major element composition of olivine and spinel (representative analyses)

	Olivine							Spinel									
Group:	I	I	II	II	III	IV	IV	I	I	I	II	II	III	III	III	IV	IV
	ol-I	ol-I	ol-I	ol-I	ol-I	ol-I	ol-I	spl-IIa	spl-IIa	spl-IIb	spl-I	spl-IIb	spl-I	spl-I	spl-I	spl-I	spl-I
Sample:	1965/4	1963/2	1958/6	1958/20	1965/1	1961/1	1968/1	1965/4	1960/2	1965/4	1958/20	1959/24	781/6	1965/1	1965/1	1961/1	1961/1
Location:	core	core	core	core	core	core	core	core	core	sympl	core	cluster core	core	core	rim	core	rim
SiO_2	41·07	40·90	40·03	40·75	41·17	41·48	41·19	0·01	n.d.	0·04	0·06	0·04	n.d.	n.d.	n.d.	n.d.	n.d.
TiO_2	n.d.	n.d.	n.d.	n.d.	0·02	n.d.	0·03	0·02	0·06	0·06	0·19	0·18	0·06	0·11	0·05	0·02	0·01
Al_2O_3	0·02	0·03	0·07	0·05	n.d.	n.d.	n.d.	57·50	51·51	63·40	56·97	53·62	52·24	39·41	41·71	43·34	54·70
Cr_2O_3	n.d.	n.d.	0·05	n.d.	n.d.	0·01	0·02	10·80	17·62	4·36	8·99	12·93	15·58	30·24	27·61	25·42	13·54
Fe_2O_3	—	—	—	—	—	—	—	0·93	0·72	0·81	3·36	3·08	2·07	0·87	1·23	0·92	1·44
FeO	10·33	10·20	11·75	10·19	8·04	7·48	9·37	9·55	10·72	8·62	7·69	8·26	8·77	11·12	10·10	11·50	8·06
MnO	0·13	0·15	0·16	0·14	0·12	0·14	0·09	0·04	0·18	0·16	0·16	0·13	0·12	0·16	0·16	0·21	0·15
NiO	0·34	0·37	0·35	0·35	0·37	0·43	0·35	0·35	0·33	0·42	0·41	0·45	0·39	0·14	0·13	0·12	0·26
MgO	48·97	48·70	47·06	48·70	50·35	51·12	49·62	20·23	18·89	21·30	21·37	20·65	20·11	17·44	18·29	17·36	20·68
CaO	0·03	0·02	0·19	0·10	0·04	0·01	0·01	n.d.	0·01	0·02	0·02	0·03	0·01	0·02	n.d.	0·01	0·01
Na_2O	0·03	n.d.	0·01	n.d.	0·03	0·03	0·02	n.a.	n.a.	n.a.	n.a.	n.a.	n.a.	n.a.	n.a.	n.a.	n.a.
K_2O	0·02	n.d.	n.d.	n.d.	n.d.	0·01	n.d.	n.a.	n.a.	n.a.	n.a.	n.a.	n.a.	n.a.	n.a.	n.a.	n.a.
ZnO	n.a.	n.a.	n.a.	n.a.	n.a.	n.a.	n.a.	0·14	0·18	0·13	0·03	0·04	0·10	0·15	0·10	0·23	0·29
Total	100·95	100·37	99·67	100·28	100·15	100·70	100·71	99·58	100·21	99·31	99·26	99·42	99·45	99·65	99·40	99·13	99·15
Stoich.	4O	4O	4O	4O	4O	4O	4O	4O	4O	4O	4O	4O	4O	4O	4O	4O	4O
Si	1·000	1·001	0·995	0·999	1·000	1·000	1·001	0·000	—	0·001	0·002	0·001	—	—	—	—	—
Ti	—	—	—	—	0·000	0·000	0·001	0·000	0·001	0·001	0·004	0·004	0·001	0·002	0·001	0·000	0·000
Al	0·001	0·001	0·002	0·001	—	0·000	—	1·759	1·613	1·893	1·740	1·661	1·630	1·305	1·366	1·421	1·691
Cr	—	—	0·001	—	—	0·000	0·000	0·222	0·370	0·087	0·184	0·269	0·326	0·672	0·606	0·559	0·281
Fe^{3+}	—	—		—	—	—	—	0·018	0·014	0·015	0·065	0·061	0·041	0·018	0·026	0·019	0·028
Fe^{2+}	0·210	0·209	0·244	0·209	0·163	0·151	0·190	0·207	0·238	0·183	0·167	0·182	0·194	0·261	0·235	0·268	0·177
Mn	0·003	0·003	0·003	0·003	0·002	0·003	0·002	0·001	0·004	0·003	0·003	0·003	0·003	0·004	0·004	0·005	0·003
Ni	0·007	0·007	0·007	0·007	0·007	0·008	0·007	0·007	0·007	0·009	0·009	0·010	0·008	0·003	0·003	0·003	0·006
Mg	1·777	1·777	1·745	1·779	1·824	1·837	1·797	0·783	0·748	0·805	0·825	0·809	0·794	0·730	0·758	0·720	0·809
Ca	0·001	0·001	0·005	0·003	0·001	0·000	0·000	—	0·000	0·001	0·001	0·001	0·000	0·001	—	0·000	0·000
Na	0·002	—	0·001	—	0·001	0·001	0·001	—	—	—	—	—	—	—	—	—	—
K	0·001	—	—	—	—	0·000	—	—	—	—	—	—	—	—	—	—	—
Zn	—	—	—	—	—	—	—	0·003	0·003	0·002	0·001	0·001	0·002	0·003	0·002	0·005	0·006
Total	3·001	2·999	3·003	3·001	3·000	3·001	2·999	3·000	3·000	3·000	3·000	3·000	3·000	3·000	3·000	3·000	3·000
Mg-no.	89·4	89·5	87·7	89·5	91·8	92·4	90·4	77·6	75·9	81·5	83·2	81·7	80·3	73·6	76·4	72·9	82·1
Cr-no.								11·2	18·7	4·4	9·6	13·9	16·7	34·0	30·7	28·2	14·2

Fe_2O_3 in spinel is calculated assuming perfect stoichiometry; n.a., not analysed; n.d., not detected; —, not calculated.

Table 3: Major element composition of orthopyroxene (representative analyses)

	Orthopyroxene																	
Group:	I	I	I	I	I	I	I	II	II	II	II	III	III	III	IV	IV	IV	IV
	opx-I	opx-I	opx-I	opx-I	opx-IIa	opx-IIa	opx-IIb	opx-I	opx-I	opx-I	opx-IIb	opx-I	opx-I	opx-I	opx-I	opx-IIa	opx-I	opx-I
Sample:	1965/4	1960/2	1963/2	1965/4	1963/2	1960/2	1960/2	1958/13	1958/13	1959/24	1959/24	1965/1	1965/1	781/6	1961/1	1961/1	1968/1	1968/1
Location:	Al-trough	Al-bulge	Al-bulge	rim	n.blast core	n.blast rim	sympl	core	rim	core	cluster core	core*	rim	core	core	n.blast core	core	rim
SiO_2	56·49	55·28	55·63	57·21	55·89	56·86	56·36	55·51	56·67	54·90	54·47	56·57	57·14	55·76	56·70	57·58	54·91	57·05
TiO_2	0·19	0·07	0·10	0·08	0·11	0·07	0·07	0·08	0·03	0·15	0·14	0·04	0·05	0·10	0·02	0·03	0·11	0·02
Al_2O_3	2·31	4·14	3·25	1·66	3·22	2·13	2·77	3·76	2·89	5·28	5·04	2·65	2·03	3·33	2·57	1·06	3·87	1·61
Cr_2O_3	0·35	0·35	0·27	0·11	0·26	0·25	0·12	0·37	0·24	0·49	0·55	0·43	0·22	0·34	0·42	0·09	0·51	0·15
FeO	6·56	6·35	6·46	6·18	6·48	6·16	6·56	6·34	5·92	6·04	6·03	5·33	5·16	5·49	4·83	5·11	5·88	6·28
MnO	0·20	0·21	0·15	0·14	0·20	0·23	0·20	0·13	0·12	0·13	0·11	0·13	0·13	0·16	0·10	0·16	0·15	0·23
NiO	n.d.	0·01	n.a.	n.a.	0·09	0·08	0·08	0·10	n.a.	0·09	n.a.	n.a.	0·11	0·05	0·07	0·08	0·12	0·01
MgO	34·28	33·19	33·89	34·70	33·44	34·36	33·92	33·57	34·27	32·60	32·45	34·73	34·92	33·89	35·17	35·99	33·47	34·66
CaO	0·43	0·32	0·28	0·24	0·38	0·27	0·30	0·38	0·57	1·06	1·07	0·51	0·32	0·49	0·36	0·18	0·37	0·29
Na_2O	0·05	0·06	0·04	0·03	0·04	0·05	0·04	0·09	0·12	0·15	0·16	0·05	0·07	0·03	0·01	0·01	0·06	0·04
K_2O	n.d.	0·01	n.d.	0·01	n.d.	n.d.	0·01	n.d.	n.d.	0·02	0·01	n.d.	n.d.	n.d.	n.d.	0·03	n.d.	n.d.
Total	100·85	99·97	100·05	100·39	100·11	100·46	100·41	100·32	100·83	100·90	100·02	100·43	100·15	99·63	100·28	100·32	99·45	100·34
Stoich.	6O	6O	6O	6O	6O	6O	6O	6O	6O	6O	6O	6O	6O	6O	6O	6O	6O	6O
Si	1·937	1·909	1·920	1·962	1·928	1·951	1·938	1·911	1·936	1·882	1·883	1·936	1·957	1·925	1·938	1·968	1·905	1·960
Ti	0·005	0·002	0·003	0·002	0·003	0·002	0·002	0·002	0·001	0·004	0·004	0·001	0·001	0·003	0·001	0·001	0·003	0·000
Al	0·093	0·169	0·132	0·067	0·131	0·086	0·112	0·153	0·116	0·213	0·206	0·107	0·082	0·136	0·104	0·043	0·158	0·065
Cr	0·009	0·010	0·007	0·003	0·007	0·007	0·003	0·010	0·006	0·013	0·015	0·012	0·006	0·009	0·011	0·002	0·014	0·004
Fe^{2+}	0·188	0·183	0·186	0·177	0·187	0·177	0·188	0·183	0·169	0·173	0·174	0·152	0·148	0·158	0·138	0·146	0·170	0·181
Mn	0·006	0·006	0·004	0·004	0·006	0·007	0·006	0·004	0·004	0·004	0·003	0·004	0·004	0·005	0·003	0·005	0·004	0·007
Ni	—	0·000	—	—	0·002	0·002	0·002	0·003	—	0·003	—	—	0·003	0·001	0·002	0·002	0·003	0·000
Mg	1·752	1·708	1·743	1·774	1·720	1·758	1·739	1·723	1·745	1·666	1·673	1·772	1·783	1·744	1·793	1·834	1·731	1·775
Ca	0·016	0·012	0·010	0·009	0·014	0·010	0·011	0·014	0·021	0·039	0·039	0·019	0·012	0·018	0·013	0·007	0·014	0·011
Na	0·003	0·004	0·003	0·002	0·002	0·003	0·002	0·006	0·008	0·010	0·011	0·003	0·004	0·002	0·001	0·000	0·004	0·003
K	—	0·001	—	0·001	—	—	0·001	—	—	0·001	0·000	—	—	—	—	0·001	—	—
Total	4·009	4·003	4·009	4·002	4·001	4·002	4·005	4·008	4·006	4·007	4·008	4·005	4·000	4·001	4·004	4·009	4·008	4·006
Mg-no.	90·3	90·3	90·3	90·9	90·2	90·9	90·2	90·4	91·2	90·6	90·6	92·1	92·3	91·7	92·8	92·6	91·0	90·8

*Analysed with defocused beam to include thin exsolution lamellae.
n.a., not analysed; n.d., not detected; —, not calculated.

Table 4: Major element composition of clinopyroxene (representative analyses)

	Clinopyroxene																	
Group:	I	I	I	I	I	I	I	II	II	II	II	II	III	III	III	IV	IV	IV
	cpx-I	cpx-I	cpx-I	cpx-I	cpx-IIa	cpx-IIa	cpx-IIb	cpx-I	cpx-I	cpx-I	cpx-I	cpx-IIb	cpx-I	cpx-I	cpx-I	cpx-I	cpx-I	cpx-IIa
Sample:	1963/2	1965/4	1960/2	1965/4	1963/2	1960/2	1960/2	1958/6	1958/13	1958/20	1958/20	1958/20	781/6	1965/1	1965/1	1961/1	1968/1	1968/1
Location:	Al-trough	Al-bulge	Al-bulge	rim	n.blast core	n.blast rim	sympl	core	core	core	rim	sympl core	core	core	rim	core	core	rim
SiO_2	53·73	52·24	51·95	52·70	52·89	52·72	52·84	50·84	52·35	51·34	51·46	51·27	52·16	53·52	54·03	53·33	52·14	53·70
TiO_2	0·64	0·81	0·65	0·53	0·66	0·46	0·65	0·67	0·40	0·46	0·50	0·49	0·29	0·12	0·10	n.d.	0·44	0·25
Al_2O_3	5·09	6·65	5·85	5·51	6·44	4·88	5·58	7·13	6·35	7·04	7·05	7·10	5·48	3·41	2·89	2·74	5·90	4·14
Cr_2O_3	0·82	1·15	0·68	0·41	0·95	0·83	0·32	0·85	0·94	1·09	0·72	0·69	1·04	1·34	0·80	0·79	1·02	0·45
FeO	2·47	2·08	1·95	2·02	2·20	2·14	2·12	4·27	2·35	3·24	3·28	3·30	2·29	2·05	1·85	1·47	2·19	2·06
MnO	0·06	0·06	0·09	0·10	0·10	0·06	0·07	0·04	0·06	0·11	0·10	0·10	0·04	0·06	0·08	0·05	n.d.	0·01
NiO	0·04	n.a.	0·05	n.a.	n.a.	n.a.	0·03	n.a.	n.a.	n.a.	n.a.	n.a.	0·02	0·03	0·05	n.d.	0·03	0·03
MgO	15·11	14·75	14·62	15·49	14·30	15·04	15·12	15·92	14·76	16·22	16·42	15·89	15·26	16·06	16·82	16·59	14·46	15·24
CaO	20·79	21·30	21·67	21·46	20·89	21·79	21·98	18·50	20·45	19·16	19·39	19·21	21·60	21·70	22·11	23·70	20·86	21·93
Na_2O	2·07	1·92	1·73	1·56	2·19	1·62	1·60	1·42	2·07	1·39	1·36	1·30	1·50	1·31	1·11	0·85	2·22	1·79
K_2O	n.d.	n.d.	0·04	0·02	n.d.	0·01	0·03	n.d.	n.d.	n.d.	0·01	0·01	n.d.	n.d.	n.d.	n.d.	n.d.	0·02
Total	100·83	100·97	99·29	99·79	100·63	99·56	100·33	99·63	99·73	100·06	100·26	99·35	99·68	99·60	99·84	99·51	99·27	99·62
Stoich.	6O	6O	6O	6O	6O	6O	6O	6O	6O	6O	6O	6O	6O	6O	6O	6O	6O	6O
Si	1·926	1·874	1·895	1·907	1·900	1·918	1·905	1·851	1·897	1·856	1·856	1·864	1·897	1·945	1·956	1·943	1·902	1·949
Ti	0·017	0·022	0·018	0·014	0·018	0·013	0·018	0·018	0·011	0·012	0·013	0·013	0·008	0·003	0·003	–	0·012	0·007
Al	0·215	0·281	0·251	0·235	0·273	0·209	0·237	0·306	0·271	0·300	0·300	0·304	0·235	0·146	0·123	0·118	0·254	0·177
Cr	0·023	0·033	0·020	0·012	0·027	0·024	0·009	0·025	0·027	0·031	0·020	0·020	0·030	0·038	0·023	0·023	0·030	0·013
Fe^{2+}	0·074	0·062	0·059	0·061	0·066	0·065	0·064	0·130	0·071	0·098	0·099	0·100	0·070	0·062	0·056	0·045	0·067	0·063
Mn	0·002	0·002	0·003	0·003	0·003	0·002	0·002	0·001	0·002	0·004	0·003	0·003	0·001	0·002	0·003	0·001	–	0·000
Ni	0·001	–	0·002	–	–	–	0·001	–	–	–	–	–	0·001	0·001	0·001	–	0·001	0·001
Mg	0·807	0·789	0·795	0·836	0·766	0·816	0·813	0·864	0·797	0·874	0·883	0·861	0·827	0·870	0·908	0·901	0·786	0·824
Ca	0·799	0·818	0·847	0·832	0·804	0·849	0·849	0·721	0·794	0·742	0·749	0·748	0·842	0·845	0·858	0·925	0·815	0·853
Na	0·144	0·134	0·122	0·109	0·153	0·114	0·112	0·100	0·145	0·097	0·095	0·092	0·106	0·092	0·078	0·060	0·157	0·126
K	–	–	0·002	0·001	–	0·001	0·001	–	–	–	0·001	0·001	–	–	–	–	–	0·001
Total	4·009	4·015	4·014	4·010	4·009	4·010	4·011	4·016	4·016	4·015	4·018	4·006	4·016	4·006	4·008	4·016	4·023	4·013
Mg-no.	91·6	92·7	93·0	93·2	92·0	92·6	92·7	86·9	91·8	89·9	89·9	89·9	92·2	93·3	94·2	95·3	92·2	92·9

n.a., not analysed; n.d., not detected; —, not calculated.

JOURNAL OF PETROLOGY VOLUME 47 NUMBER 11 NOVEMBER 2006

Table 5: *Representative major element composition of Ti-pargasite and phlogopite*

	Ti-pargasite							Phlogopite	
Group:	I	I	I	I	I	I	I	I	I
	amph-i	amph-i	amph-i	amph-i	amph-ii	amph-ii	amph-iii	phl	phl
Sample:	1960/2	1963/2	1963/2	1965/4	1965/4	1963/2	1963/2	1963/2	1963/2
Location:	core	core	rim	core	within sympl	within sympl	repl. cpx	core	rim
SiO_2	42·86	43·41	43·82	43·74	43·56	43·94	43·55	38·59	38·74
TiO_2	2·89	2·84	2·75	3·56	2·50	3·40	2·78	4·71	4·76
Al_2O_3	14·45	14·55	14·58	13·69	14·46	13·96	13·61	15·52	15·24
Cr_2O_3	0·51	0·69	0·44	0·71	0·67	0·38	1·03	0·89	0·88
FeO	3·64	3·82	3·58	3·57	3·52	3·58	3·42	3·90	3·92
MnO	0·09	0·09	0·06	0·03	0·07	0·07	0·06	0·01	0·01
NiO	0·22	0·10	0·10	0·10	0·12	0·09	0·07	0·26	0·24
MgO	17·23	16·85	17·53	17·86	18·12	17·57	17·75	21·58	21·90
CaO	11·61	11·21	11·31	11·37	11·59	11·64	11·55	0·04	0·04
Na_2O	3·34	3·56	3·43	3·49	3·57	3·72	3·65	0·94	0·92
K_2O	0·74	1·01	0·74	0·21	0·06	0·13	0·35	9·43	9·15
F	n.a.	0·05	n.d.	0·05	n.d.	0·03	n.a.	n.a.	n.a.
Cl	n.a.	n.a.	n.a.	0·02	0·01	n.a.	n.a.	n.a.	n.a.
H_2O*	2·10	2·09	2·13	2·10	2·13	2·12	2·11	4·23	4·24
Total†	99·67	100·25	100·48	100·48	100·38	100·61	99·94	100·09	100·03
Stoich.	23O	23O	23O	23O	23O	23O	23O	22O	22O
Si	6·110	6·155	6·173	6·161	6·137	6·177	6·178	5·464	5·481
Ti	0·310	0·303	0·291	0·378	0·265	0·359	0·297	0·502	0·506
Al	2·427	2·432	2·421	2·272	2·401	2·314	2·276	2·590	2·541
Cr	0·057	0·078	0·049	0·079	0·075	0·042	0·115	0·100	0·099
Fe^{2+}	0·434	0·453	0·422	0·421	0·415	0·421	0·406	0·462	0·464
Mn	0·011	0·010	0·008	0·004	0·009	0·008	0·007	0·001	0·001
Ni	0·026	0·012	0·012	0·011	0·014	0·010	0·008	0·029	0·027
Mg	3·661	3·561	3·682	3·749	3·805	3·683	3·754	4·555	4·618
Ca	1·773	1·703	1·707	1·716	1·749	1·754	1·756	0·006	0·006
Na	0·923	0·979	0·938	0·952	0·975	1·015	1·004	0·257	0·253
K	0·134	0·183	0·133	0·038	0·012	0·023	0·064	1·703	1·651
F	—	0·021	—	0·022	—	0·011	—	—	—
Cl	—	—	—	0·005	0·002	—	—	—	—
H	2·000	1·979	2·000	1·973	1·998	1·989	2·000	4·000	4·000
Total‡	15·867	15·868	15·837	15·781	15·855	15·805	15·864	15·669	15·646
Mg-no.	89·4	88·7	89·7	89·9	90·2	89·7	90·2	90·8	90·9
Cr-no.	2·29	3·10	2·00	3·36	3·01	1·77	4·83	3·72	3·74

*Calculated based on stoichiometry.
†Corrected for F and Cl.
‡Without F, Cl, and H.
n.a., not analysed; n.d., not detected; —, not calculated.

Amphiboles from Group III samples are Ti-poor magnesiokatophorites with high Na_2O and relatively low K_2O contents (3·66–5·65 and 0·23–0·52 wt %, respectively), and high Mg-numbers (91·3–93·0). The associated phlogopite is also Ti-poor (≤0·5 wt %), and characterized by very high NaO_2 contents (Kaeser *et al.*, in preparation).

Major element zoning

Mineral zoning was investigated by electron microprobe traverses across single grains. Representative zoning patterns for pyroxene are illustrated in Figs 5a–e and 6a–e. Representative core and rim values for all analysed samples are given in the supplementary dataset (at http://www.petrology.oupjournals.org/).

Table 6: Calculated garnet and pyroxene compositions obtained from reintegration (for explanation, see the Analytical Methods section)

	Garnet (recalculated)						Orthopyroxene (EMP scan)						Clinopyroxene (recalculated)					
Group:	I		I		I		I		I		IV		I		I		IV	
	(grt-I)		(grt-I)		(grt-I)		opx-I		opx-I		opx-I		cpx-I		cpx-I		cpx-I	
Sample:	1960/2		1963/2		1965/4		1960/2		1963/2		1961/1		1960/2		1963/2		1961/1	
Remark:	bulk		bulk		bulk		tiny cpx		tiny cpx		opx + spl		opx		opx		opx + spl	
	sympl.	2σ	sympl.	2σ	sympl.	2σ	lamellae	2σ	lamellae	2σ	lamellae	2σ	lamellae	2σ	lamellae	2σ	lamellae	2σ
SiO_2	41·76	0·18	41·50	0·17	41·10	0·35	56·05	0·14	56·22	0·14	56·31	0·49	53·01	0·23	53·83	0·11	52·48	0·00
TiO_2	0·21	0·03	0·24	0·11	0·23	0·14	0·13	0·02	0·16	0·01	0·01	0·01	0·49	0·06	0·64	0·02	0·03	0·19
Al_2O_3	24·82	0·40	25·16	0·44	25·54	0·38	2·53	0·05	2·56	0·12	2·79	0·30	4·21	0·07	4·93	0·10	3·37	0·18
Cr_2O_3	1·82	0·14	1·36	0·13	2·20	0·11	0·37	0·05	0·25	0·01	0·55	0·24	1·24	0·06	0·83	0·04	1·17	0·13
FeO	5·55	0·12	5·25	0·09	5·29	0·10	6·30	0·14	6·57	0·04	4·87	0·18	2·67	0·06	2·81	0·01	1·64	0·05
MnO	0·13	0·03	0·12	0·03	0·10	0·03	0·17	0·03	0·16	0·02	0·13	0·03	0·09	0·02	0·09	0·01	0·08	0·03
NiO	0·05	0·00	0·05	0·00	0·00	0·00	0·09	0·04	0·08	0·02	0·10	0·05	0·05	0·03	0·04	0·02	0·01	0·00
MgO	19·97	0·41	18·70	0·33	19·19	0·39	33·63	0·13	34·09	0·10	34·61	0·39	16·58	0·19	16·16	0·03	17·27	0·00
CaO	5·39	0·05	6·74	0·20	6·12	0·07	0·53	0·07	0·57	0·11	0·67	0·53	19·75	0·29	19·56	0·33	22·66	0·46
Na_2O	0·40	0·02	0·53	0·12	0·41	0·13	0·05	0·02	0·06	0·01	0·03	0·02	1·63	0·25	1·96	0·20	0·81	0·52
K_2O	0·01	0·02	0·01	0·01	0·01	0·01	0·01	0·01	0·01	0·00	0·01	0·01	0·01	0·02	0·01	0·02	0·01	0·01
Total	100·11		99·64		100·19		99·86		100·72		100·08		99·73		100·84		99·52	
Stoich.	12O		12O		12O		6O		6O		6O		6O		6O		6O	
Si	2·937		2·937		2·895		1·939		1·931		1·932		1·922		1·926		1·913	
Ti	0·011		0·013		0·012		0·003		0·004		0·000		0·013		0·017		0·001	
Al	2·057		2·098		2·120		0·103		0·104		0·113		0·180		0·208		0·145	
Cr	0·101		0·076		0·123		0·010		0·007		0·015		0·036		0·023		0·034	
Fe	0·326		0·310		0·311		0·182		0·189		0·140		0·081		0·084		0·050	
Mn	0·008		0·007		0·006		0·005		0·005		0·004		0·003		0·003		0·002	
Ni	0·003		0·003		0·000		0·002		0·002		0·003		0·002		0·001		0·000	
Mg	2·094		1·972		2·015		1·734		1·745		1·771		0·896		0·862		0·939	
Ca	0·406		0·511		0·462		0·019		0·021		0·025		0·767		0·750		0·885	
Na	0·055		0·072		0·056		0·004		0·004		0·002		0·114		0·136		0·057	
K	0·001		0·001		0·001		0·000		0·000		0·000		0·000		0·000		0·000	
Total	8·001		8·000		8·000		4·003		4·012		4·004		4·014		4·009		4·025	
Mg-no.	86·5		86·4		86·6		90·5		90·2		92·7		91·7		91·1		95·0	
Cr-no.	4·68		3·49		5·47		–		–		–		–		–		–	

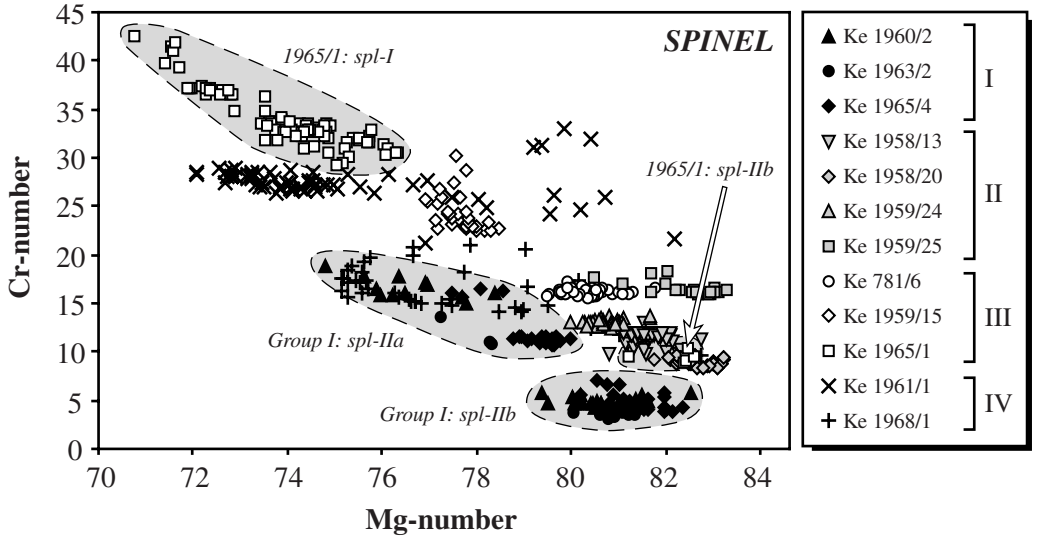

Fig. 3. Variation of Cr-number [molar Cr/(Cr + Al + Fe^{3+})] vs Mg-number [molar Mg/(Mg + Fe^{2+})] in spinel. Fe^{3+} calculated assuming perfect stoichiometry. Compositionally different spinel generations (when present) are highlighted by grey fields.

In Group I samples, opx-I typically shows Al zoning patterns with a low-concentration plateau in the core and increasing values toward the rims (Fig. 5a). The alumina peak is typically associated with a drastic decrease of concentration within the outermost rim (Fig. 5a; hereafter termed the 'Al bulge'). Ca and Cr show plateaux in the cores and outer zones with lower concentrations. Neoblasts (opx-IIa) lack the central Al trough, but show the Al bulge (Fig. 5b). Their Ca concentrations correspond to those of opx-I rims and show no zoning. Al and Cr in cpx-I grains show similar patterns to opx-I (Fig. 6a and b). Ca and Mg-number profiles are flat or display a slight rimward increase (Fig. 6a–c), with rim compositions corresponding to the core composition of cpx-IIa (Fig. 6c). Ti and Na patterns either are flat or show slightly decreasing values from cores to rims (Fig. 6a and b). Spinel and olivine are not zoned with respect to major elements.

In contrast to Group I, strongly recrystallized (grt)–spl-lherzolites (Ke 1958/20 and 1959/24) show much more homogeneous grains. Zoning in pyroxenes is generally absent (Figs 5d and 6d), but some clinopyroxene grains show Cr contents decreasing from core to rim (Table 4 and supplementary dataset). There is no difference in composition between larger and smaller grains. Orthopyroxene from the xenolith with a tabular fabric (Ke 1958/13) shows decreasing Al content from core to rim, accompanied by increasing Ca content (Fig. 5c).

Al contents in opx-I grains from Group III spl-harzburgites decrease from a central plateau towards the rims, whereas Ca and Cr patterns are either flat or decrease towards the rims (Fig. 5e). With the exception of Al and Cr, which decrease rimwards, clinopyroxene is not zoned (Fig. 6e). Large Cr spinel grains (spl-I) show a slight decrease in Cr-number (and increase in Mg-number) from core to rim (not shown).

Al zoning patterns in large opx-I clasts in the Group IV spl-lherzolite (Ke 1968/1) show decreasing values from core to rim (Table 3). The patterns for all other elements are flat. Both cpx-I and opx-I in the ultramylonitic spl-harzburgite (Ke 1961/1) are compositionally homogeneous but contain abundant lamellae of pyroxene (clinopyroxene in opx-I and vice versa) and Cr spinel. Considerable zoning was found in spl-I (Table 2) as well as in olivine. Mg-numbers in spl-I increase from core to rim whereas Cr-numbers show the opposite trend. In the ultramylonitic sample (Ke 1961/1), Cr-numbers again strongly increase within the outermost 20 μm. Ca contents are higher in olivine rims than in cores, whereas Mg-numbers decrease towards the rim.

Trace elements

Representative LA-ICPMS data for all analysed minerals is given in Tables 7–9. Trace element signatures are shown in Figs 7–10. The complete dataset is available for downloading at http://www.petrology.oupjournals.org/.

Clinopyroxene

Group I cpx-I and IIa are characterized by light rare earth element (LREE) depletion (Fig. 7b) with low $(La/Sm)_N$ values (Fig. 8), similar to the clinopyroxene in fertile lherzolites (Eggins *et al.*, 1998). Strong compositional zoning was found with respect to the heavy rare earth elements (HREE). Exsolved cores of clinopyroxene

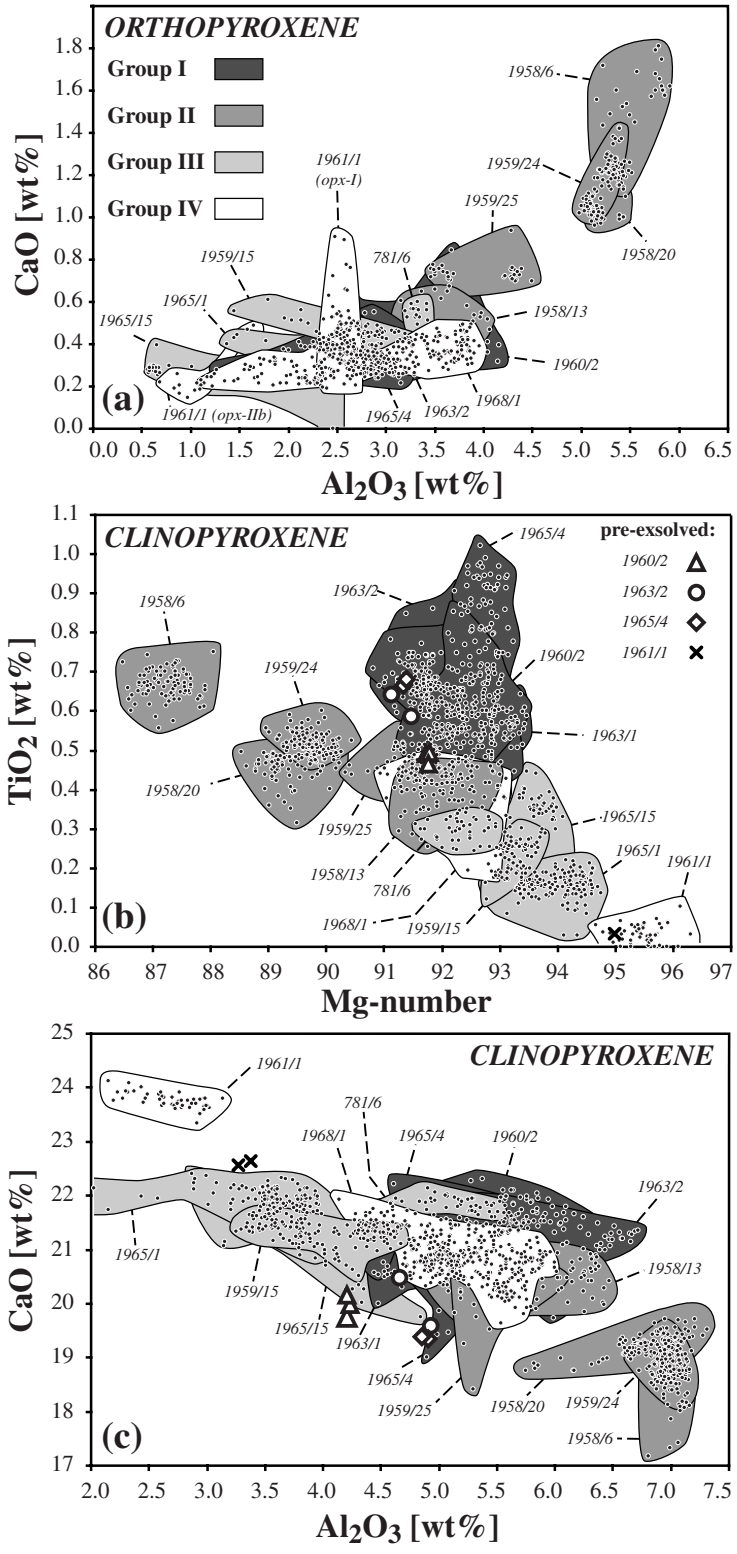

Fig. 4. Major element composition of orthopyroxene and clinopyroxene in the peridotite xenoliths of Marsabit. (a) Al_2O_3 vs CaO contents of orthopyroxene; (b) Mg-number vs TiO_2 contents of clinopyroxene; (c) Al_2O_3 vs CaO contents of clinopyroxene. Dots indicate individual analyses; grey-shaded fields attribute them to the four textural groups (I, II, III, IV). Corresponding sample numbers are indicated in italics. Large symbols in (b) and (c) represent recalculated clinopyroxene compositions prior to orthopyroxene and spinel exsolution (see text for further explanation).

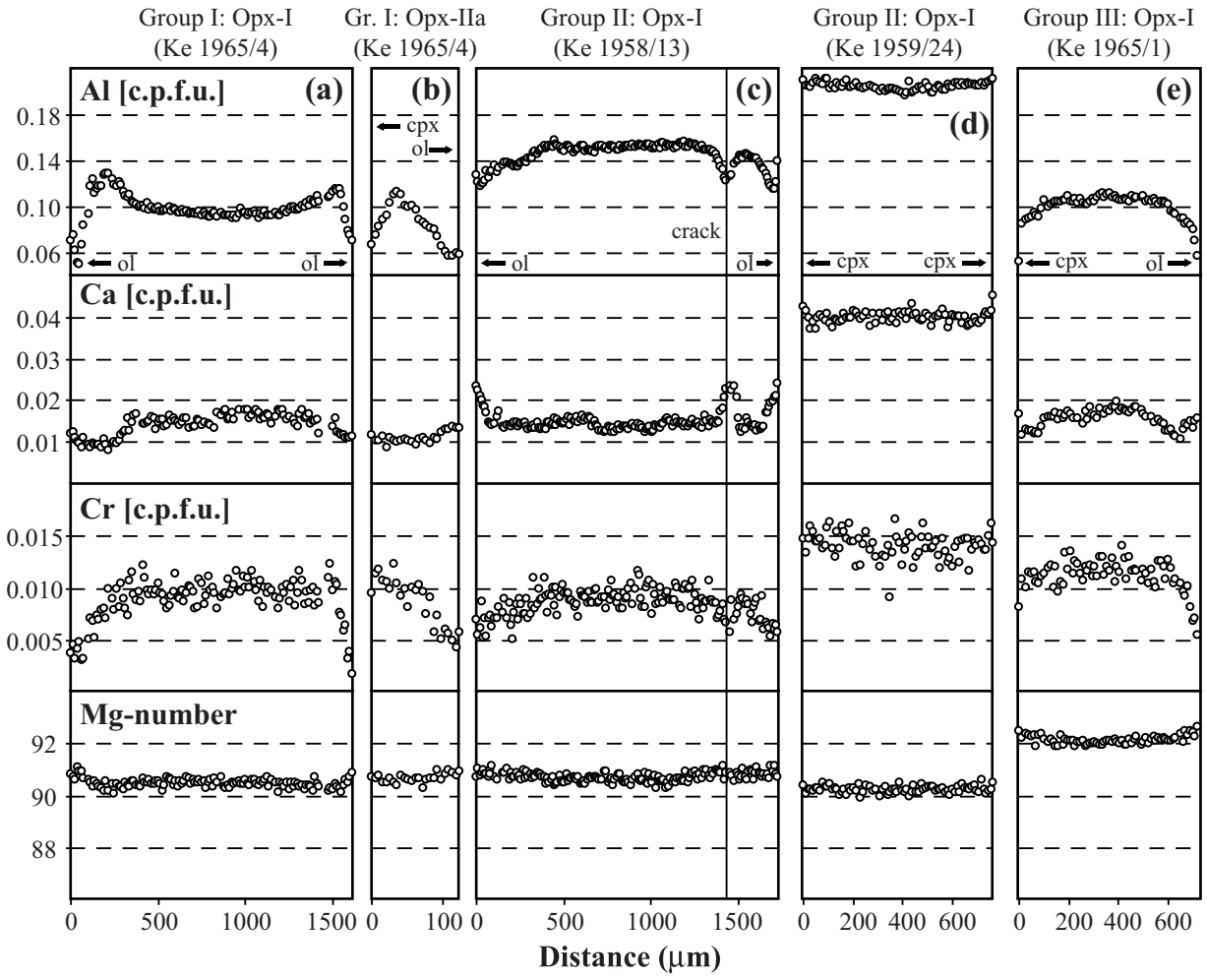

Fig. 5. Major element zoning patterns in orthopyroxene (distance is rim–core–rim; c.p.f.u., cations per formula unit): (a) opx-I porphyroclast in Ke 1965/4 (Group I); (b) opx-IIa neoblast in Ke 1965/4 (Group I); (c) opx-I in tabular–granuloblastic Ke 1958/13 (Group II); (d) opx-I in equilibrated Ke 1959/24 (Group II); (e) opx-I porphyroclast in Ke 1965/1 (Group III).

have very low HREE contents [$(Eu/Lu)_N \geq 3{\cdot}18$], whereas the rims show flat patterns [$(Eu/Lu)_N \sim 1$; Fig. 8]. HREE contents in the cores of cpx-IIa are similar to those in cpx-I rims (Fig. 7b). Extended trace element patterns (Fig. 7a) exhibit negative Nb and Ta anomalies. Negative Zr, Hf, and Ti anomalies occur but are often only moderately developed, whereas some rim analyses have marked positive Zr and Hf anomalies (Fig. 7a).

Patterns from middle rare earth element (MREE) to HREE in Group II clinopyroxene are flat [$(Eu/Lu)_N = 1{\cdot}05–1{\cdot}75$; Fig. 8] and HREE zoning is not observed. LREE, on the other hand, show variable patterns ranging from depleted to enriched (Figs 7c and d, and 8). LREE enrichment is accompanied by higher U and Th abundances. The most enriched signature is observed in clinopyroxene of Ke 1958/13, characterized by its weak tabular fabric (Fig. 7c and d). Negative Zr, Hf and Ti anomalies are broadly the same as in Group I clinopyroxene.

The investigated Group III xenolith (Ke 1965/1) contains clinopyroxene variably enriched in LREE (Fig. 7e) with $(La/Sm)_N$ values of the same order of magnitude as in the more recrystallized samples from Group II (Fig. 8). The HREE, on the other hand, show a similar variation as in Group I clinopyroxene, depending on whether they occur close to or far from rare symplectites (Fig. 7f). U and Th contents are high (Fig. 7e). Negative Zr, Hf and Ti anomalies are more marked than in Group I and II clinopyroxene.

Clinopyroxenes from the mylonitic spl-lherzolite (Ke 1968/1) are similar to those of Group I samples (Fig. 7g). REE patterns are convex-upward (Fig. 7h), whereas no compositional differences between porphyroclasts and neoblasts are observed. Trace element

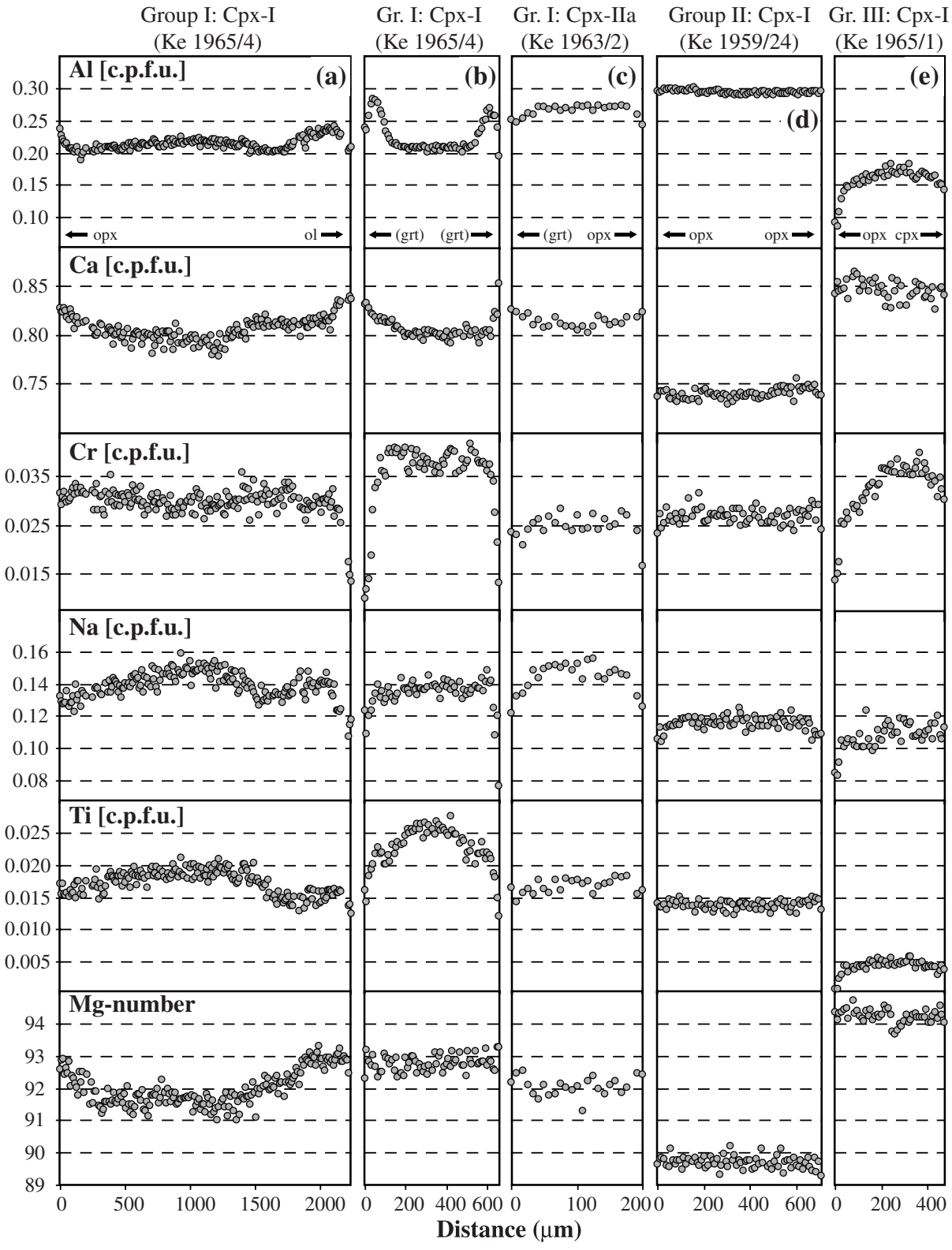

Fig. 6. Major element zoning patterns in clinopyroxene (distance is rim–core–rim; c.p.f.u., cations per formula unit): (a) cpx-I porphyroclast in Ke 1965/4 (Group I); (b) cpx-I (euhedral inclusion in symplectite) in Ke 1965/4 (Group I); (c) cpx-IIa neoblast in Ke 1963/2 (Group I); (d) cpx-I in equilibrated Ke 1959/24 (Group II); (e) cpx-I porphyroclast in Ke 1965/1 (Group III).

Table 7: Representative trace element composition of clinopyroxene (in μg/g)

	Group I						Group II				Group III		Group IV	
Sample:	1963/2	1963/2	1963/2	1963/2	1965/4	1965/4	1958/13	1958/20	1959/24	1959/25	1965/1	1965/1	1961/1	1968/1
Location:	cpx-I, core	cpx-I, core	cpx-I, rim	cpx-IIa, core	cpx-I, core	cpx-I, rim	cpx-I, core	cpx-I, core	cpx-I, core	cpx-I, core	cpx-I, core	cpx-I, rim	cpx-I, core	cpx-I, core
Analysis no.:	dd08b06	ob29d13	ob29d10	ob29d08	ob28c11	ob28c07	ob29a10	ob29b07	ob28b10	ob28a03	mc22a13	ob28d12	mc22c05	mc22b10
P	30·5	29·0	46·7	35·3	33·3	85·4	53·1	47·4	48·0	25·3	17·9	19·5	11·6	20·3
K	0·86	<0·60	3·20	1·39	1·99	<5·90	4·77	21·7	18·0	<0·68	0·72	<0·78	7·44	0·97
Sc	26·4	23·9	50·9	40·1	27·5	172·7	66·9	55·3	48·9	47·2	141	104	66·2	53·4
Ti	3180	3424	3372	3303	3648	4726	2277	2617	2747	2584	837	998	156	2274
V	326	335	314	326	330	297	259	228	246	294	202	250	178	253
Ni	270	276	231	228	276	277	298	348	364	346	263	290	269	268
Zn	3·86	4·87	3·05	2·72	6·66	3·78	6·18	12·1	14·3	11·0	4·81	6·22	22·1	5·42
Ga	n.a.	8·93	5·34	6·45	8·98	3·14	3·16	4·53	5·00	4·10	1·34	1·54	0·88	3·13
Rb	0·008	<0·009	<0·011	<0·008	<0·010	<0·080	<0·009	0·011	0·012	<0·010	0·010	<0·012	0·043	0·011
Sr	68·6	67·8	57·7	52·8	74·1	50·2	117	113	84·2	53·9	39·6	67·8	33·3	52·6
Y	3·12	3·93	18·8	15·2	3·37	69·6	16·0	14·8	14·6	13·8	41·2	13·1	3·52	5·97
Zr	25·4	21·9	36·1	29·2	23·2	102	40·1	27·4	27·1	19·9	22·3	12·5	21·5	16·9
Nb	0·065	0·105	0·066	0·048	0·23	0·047	0·33	1·20	0·71	0·053	0·072	0·031	0·084	0·038
Cs	<0·004	<0·002	<0·003	<0·003	<0·004	<0·031	<0·002	0·002	0·003	<0·002	0·003	<0·004	0·004	0·006
Ba	<0·021	<0·011	<0·015	0·024	<0·021	<0·108	0·017	0·083	0·057	0·020	0·129	0·255	0·157	<0·014
La	0·99	0·84	0·94	0·81	1·05	0·83	5·99	4·77	1·23	0·82	0·79	4·14	0·20	0·48
Ce	3·62	3·60	3·63	3·16	3·60	2·47	10·4	10·6	3·79	2·54	2·15	5·61	0·917	2·23
Pr	0·75	0·67	0·67	0·59	0·69	0·46	1·18	1·24	0·72	0·48	0·32	0·50	0·29	0·48
Nd	4·66	4·20	4·18	3·99	4·17	3·19	5·61	5·56	4·51	3·20	1·83	2·24	2·97	2·83
Sm	1·42	1·63	1·74	1·74	1·62	2·19	1·76	1·51	1·78	1·40	0·98	0·78	1·84	1·28
Eu	0·58	0·55	0·82	0·75	0·59	0·90	0·82	0·72	0·78	0·66	0·64	0·38	0·55	0·48
Gd	1·42	1·42	2·42	2·14	1·44	6·02	2·11	2·12	2·14	1·93	2·74	1·13	1·01	1·30
Tb	n.a.	0·19	0·48	0·40	0·21	1·54	0·42	0·38	0·43	0·40	0·74	0·25	0·11	0·23
Dy	0·93	1·04	3·20	2·57	0·98	10·8	2·92	2·80	2·70	2·35	6·50	2·09	0·73	1·37
Ho	0·13	0·14	0·74	0·58	0·15	2·89	0·67	0·58	0·57	0·53	1·61	0·51	0·13	0·23
Er	0·27	0·29	2·01	1·76	0·24	8·37	1·93	1·54	1·45	1·35	5·04	1·47	0·41	0·55
Tm	0·037	0·042	0·34	0·24	0·025	1·13	0·24	0·24	0·24	0·20	0·76	0·25	0·059	0·084
Yb	0·19	0·21	2·17	1·78	0·25	6·83	1·87	1·53	1·61	1·35	5·42	1·71	0·52	0·52
Lu	0·017	0·040	0·27	0·26	0·009	1·00	0·24	0·20	0·20	0·20	0·81	0·21	0·075	0·061
Hf	1·10	0·79	1·15	0·99	1·00	3·05	0·96	0·78	0·78	0·68	0·41	0·32	0·34	0·58
Ta	0·017	0·018	0·006	0·012	0·019	<0·033	0·064	0·10	0·050	0·006	0·015	0·009	0·021	0·006
Pb	0·18	0·16	0·17	0·15	0·16	<0·39	0·23	0·098	0·073	0·11	0·38	0·72	0·52	0·085
Th	0·022	0·012	0·009	0·009	0·017	<0·015	0·80	0·15	0·18	0·042	0·014	0·64	0·003	0·005
U	0·004	0·009	0·006	0·006	0·006	0·016	0·191	0·037	0·040	0·013	0·010	0·35	0·007	0·004

n.a., not analysed.

Table 8: Representative trace element composition of orthopyroxene, Ti-pargasite, and phlogopite (in μg/g)

	Opx, Group I		Opx, Group II				Opx, Group III		Opx, Group IV		Ti-parg, Group I			Phl, G.I
Sample:	1963/2	1965/4	1958/13	1958/20	1959/24	1959/25	1965/1	1965/1	1961/1	1968/1	1963/2	1965/4	1963/2	1963/2
Location:	opx-I, core	opx-I, core	opx-I, core	opx-I, core	opx-I, core	opx-I, core	opx-I, core	opx-I, core	opx-I, core	opx-I, core	amph-i	amph-ii	amph-iii	core
Analysis no.:	ob28f06	ob28c10	ob29a04	ob29b12	ob28b07	ob28a05	mc22a12	mc22a09	mc22c11	mc22b13	dd08b13	ob28c05	ob29d04	ob28f09
P	22·3	13·7	20·4	19·8	24·5	16·6	16·7	11·1	12·8	9·39	118	257	137	21·5
K	0·72	0·50	<0·61	<0·47	0·56	<0·58	<0·46	<0·48	<0·50	<0·48	8614	556	4109	82709
Sc	5·17	9·29	10·9	18·9	15·4	14·3	50·9	23·9	18·5	7·08	61·3	139	55·9	2·98
Ti	863	879	443	763	796	555	177	263	56·4	352	15013	12194	17163	23896
V	72·8	69·4	74·3	105	97·7	87·4	48·8	70·2	75·5	68·5	396	270	475	330
Ni	622	562	594	773	760	723	600	592	591	566	745	915	884	1773
Zn	16·0	19·0	22·8	44·0	46·5	37·6	30·0	25·2	23·7	21·1	4·36	13·1	6·77	8·98
Ga	4·19	2·18	2·10	4·65	4·36	3·42	0·71	1·45	0·96	1·96	n.a.	2·28	5·18	6·64
Rb	<0·008	<0·013	<0·011	<0·009	0·002	0·024	<0·007	<0·006	<0·005	<0·005	2·13	0·50	0·73	106
Sr	0·27	0·057	0·094	0·66	0·44	0·10	0·021	0·041	0·095	0·035	157	131	153	33·5
Y	0·38	0·58	0·54	1·25	1·22	0·89	1·64	0·84	0·18	0·12	27·0	112	39·1	0·13
Zr	0·68	0·44	0·90	2·41	2·24	1·04	0·96	0·42	1·15	0·17	36·9	71·5	41·6	2·04
Nb	0·005	<0·004	0·021	0·065	0·044	0·006	0·010	0·012	0·009	0·007	7·70	6·44	2·44	2·66
Cs	<0·002	<0·003	<0·001	<0·002	<0·002	<0·004	<0·001	0·005	<0·003	<0·002	<0·008	<0·093	<0·016	1·29
Ba	0·021	0·018	<0·012	0·026	<0·014	<0·011	<0·016	<0·017	0·039	<0·015	24·2	7·45	12·8	626
La	0·007	<0·003	<0·003	0·021	0·005	0·004	0·002	<0·002	<0·003	<0·002	1·65	1·38	1·70	0·008
Ce	0·022	0·004	0·014	0·10	0·034	0·007	0·008	0·004	0·005	0·002	5·51	3·25	6·19	0·007
Pr	0·002	0·002	0·002	0·015	0·011	0·004	0·005	0·002	0·003	0·002	1·11	0·52	1·09	<0·002
Nd	<0·010	0·011	0·009	0·048	0·030	<0·014	0·008	<0·006	0·015	<0·007	6·66	4·51	7·43	0·015
Sm	<0·006	<0·013	0·021	<0·014	0·054	0·021	<0·011	<0·007	<0·009	<0·015	2·62	3·08	3·20	<0·013
Eu	0·005	0·002	0·006	0·020	0·023	0·004	0·009	0·006	0·009	0·003	1·15	1·75	1·29	0·014
Gd	0·020	0·037	0·021	0·038	0·107	0·031	0·023	0·009	0·022	0·015	3·44	9·24	4·91	<0·015
Tb	0·007	0·007	0·008	0·010	0·015	0·013	0·009	0·008	0·004	0·003	n.a.	2·04	0·87	0·005
Dy	0·048	0·052	0·056	0·172	0·182	0·126	0·162	0·056	0·034	0·013	4·57	17·6	6·27	0·017
Ho	0·011	0·029	0·025	0·047	0·041	0·032	0·062	0·028	0·004	0·006	1·07	4·46	1·56	0·005
Er	0·056	0·057	0·088	0·15	0·16	0·11	0·30	0·14	0·010	<0·005	2·81	11·8	4·29	0·009
Tm	0·008	0·019	0·018	0·036	0·026	0·019	0·066	0·035	0·009	0·003	0·40	1·66	0·61	0·003
Yb	0·090	0·23	0·15	0·29	0·21	0·23	0·69	0·33	0·064	0·025	2·46	10·8	4·16	<0·015
Lu	0·014	0·037	0·035	0·044	0·046	0·037	0·15	0·066	0·013	0·009	0·36	1·56	0·52	0·002
Hf	0·015	0·011	0·045	0·089	0·075	0·028	0·011	0·013	0·022	0·007	1·10	1·65	1·41	0·049
Ta	<0·002	<0·001	<0·002	0·004	0·003	<0·002	<0·001	0·002	<0·002	<0·001	0·15	0·17	0·08	0·13
Pb	0·043	<0·036	0·041	0·033	0·035	0·048	0·021	0·022	0·022	0·014	0·69	<0·93	0·38	0·46
Th	<0·001	0·002	<0·003	0·003	0·002	<0·002	0·002	<0·003	<0·002	0·003	0·012	<0·037	<0·010	0·002
U	0·001	<0·002	0·007	<0·002	0·004	<0·001	0·002	<0·001	<0·002	<0·002	0·008	<0·052	0·015	<0·002

n.a., not analysed.

Table 9: Representative trace element composition of olivine and spinel (in μg/g)

	Ol, G.I	Ol, G.II		Ol, Group III		OL, Group IV		Spl, G.I	Spl, Group II		Spl, Group III		Spl, Group IV	
Sample:	1963/2	1958/20	1959/24	1965/1	1965/1	1961/1	1968/1	1963/2	1958/20	1959/24	1965/1	1965/1	1961/1	1968/1
Location:	ol-I, core	ol-I, rim	ol-I, rim	ol-I, core	ol-I, core	ol-I, core	ol-I, core	spl-IIb	spl-I	spl-IIb	spl-I, core	spl-I, core	spl-I, core	spl-I, core
Analysis no.:	ob28f07	ob29b04	ob28b04	mc22a08	mc22a11	mc22c08	mc22b05	ob29d11	ob29b10	ob28b11	ob28d03	mc22a18	mc22c17	mc22b17
Na	14·5	64·8	80·8	17·0	8·46	16·2	6·68	0·50	95·3	3·55	1·19	237	1·91	0·92
Al	21·2	190	213	29·3	30·5	19·1	38·4	341218	307611	306716	246509	222744	264706	290093
P	45	67·5	57·2	26·0	18·4	13·8	30·7	20·7	19·9	19·6	24·2	17·3	18·1	13·2
K	<0·38	<0·36	0·33	0·60	<0·46	0·87	0·58	<112	729	12·4	<81·9	995	<50	<42·9
Ca	121	722	715	185	200	304	33·8	<2·49	2·79	0·32	<1·83	11·9	<1·68	2·32
Sc	0·72	2·91	2·62	2·47	5·19	1·63	0·70	<0·093	0·70	0·58	0·61	2·35	0·38	0·11
Ti	9·23	24·0	36·6	3·25	2·18	1·33	3·26	162	892	1031	560	447	75·1	164
V	1·20	4·16	4·37	1·29	0·86	0·56	0·62	242	363	417	832	540	663	424
Ni	2768	2462	2624	2895	2924	3011	2871	4298	3376	3092	1510	1598	1302	2402
Zn	18·7	57·2	66·5	37·9	49·9	21·4	20·1	1166	764	878	1577	1426	1812	1885
Ga	0·014	0·063	0·11	0·036	<0·01	0·047	0·041	93·7	76·4	90·5	54·3	25·4	23·2	71·2
Rb	<0·004	<0·008	0·002	0·008	<0·005	0·009	0·010	0·056	0·027	0·038	0·061	0·18	0·029	0·042
Sr	<0·002	0·009	0·012	0·004	0·003	0·056	0·006	0·059	0·52	0·037	0·062	0·45	0·095	0·054
Y	0·004	0·071	0·061	0·018	0·047	<0·003	<0·002	<0·008	0·021	0·019	0·023	0·074	0·039	0·024
Zr	0·006	0·034	0·062	0·024	0·028	0·028	0·016	0·078	0·15	0·21	0·38	1·46	0·44	0·29
Nb	<0·003	0·009	0·008	<0·003	0·005	<0·002	<0·002	0·091	0·21	0·21	0·58	0·40	0·32	0·18
Cs	<0·001	0·004	0·001	0·007	0·006	0·003	0·003	<0·013	0·013	0·051	0·073	0·58	0·026	0·046
Ba	<0·014	0·009	0·003	<0·015	<0·019	<0·017	<0·010	<0·045	<0·030	<0·04	0·081	0·31	0·41	0·046
La	<0·001	0·008	0·001	0·003	<0·001	<0·002	<0·003	0·010	0·026	0·029	0·033	0·070	0·036	0·026
Ce	0·001	0·006	<0·001	0·007	<0·002	<0·003	<0·003	0·045	0·20	0·10	0·043	0·18	0·056	0·042
Pr	<0·001	0·001	0·002	0·005	0·002	0·002	0·002	<0·011	0·019	0·016	0·053	0·033	0·029	0·029
Nd	0·004	<0·011	0·002	0·019	<0·009	0·007	<0·006	<0·076	0·060	0·022	<0·033	0·051	<0·023	<0·038
Sm	<0·005	<0·008	0·002	<0·006	<0·006	0·006	<0·007	<0·053	<0·021	0·006	0·077	0·041	0·031	<0·045
Eu	<0·001	<0·003	<0·004	<0·003	<0·002	<0·002	0·003	0·015	0·009	0·031	0·036	0·037	<0·008	0·025
Gd	<0·005	0·006	0·005	<0·006	<0·008	0·006	<0·007	<0·043	<0·021	0·011	<0·021	0·026	<0·043	0·074
Tb	<0·001	<0·001	<0·0008	0·001	<0·001	<0·001	0·004	<0·008	0·005	0·003	0·014	0·016	0·010	0·005
Dy	<0·003	0·012	0·005	0·007	0·004	<0·003	<0·004	<0·026	<0·013	<0·018	0·036	0·019	0·028	<0·013
Ho	0·001	0·003	0·001	0·004	0·003	0·001	<0·001	<0·005	0·009	0·005	0·006	0·031	0·005	0·012
Er	<0·006	0·011	0·010	<0·008	0·007	<0·003	<0·005	<0·044	<0·044	0·009	<0·024	0·066	<0·016	<0·014
Tm	<0·001	0·003	0·004	0·002	0·004	0·001	0·004	<0·004	<0·005	0·014	<0·006	0·020	0·006	0·009
Yb	0·007	0·022	0·021	0·020	0·039	0·006	<0·010	<0·052	<0·020	0·030	<0·030	0·053	<0·044	<0·049
Lu	0·001	0·010	0·007	0·005	0·013	0·001	<0·002	<0·005	0·004	0·012	<0·006	0·016	0·012	0·004
Hf	<0·003	<0·006	0·004	<0·006	0·006	<0·006	<0·004	<0·018	<0·017	0·020	<0·018	0·28	0·053	0·029
Ta	0·002	<0·002	<0·001	0·002	0·003	0·001	0·006	<0·006	0·006	0·015	0·031	0·032	0·011	0·020
Pb	0·035	0·026	0·019	0·019	0·036	0·025	0·018	<0·12	0·24	0·10	0·38	0·72	0·10	0·11
Th	<0·001	<0·001	0·002	0·004	0·002	0·002	<0·001	0·009	<0·008	0·023	0·027	0·045	0·017	0·022
U	<0·001	<0·002	<0·002	0·007	<0·002	0·001	0·002	<0·007	0·012	0·011	0·052	0·072	0·058	0·043

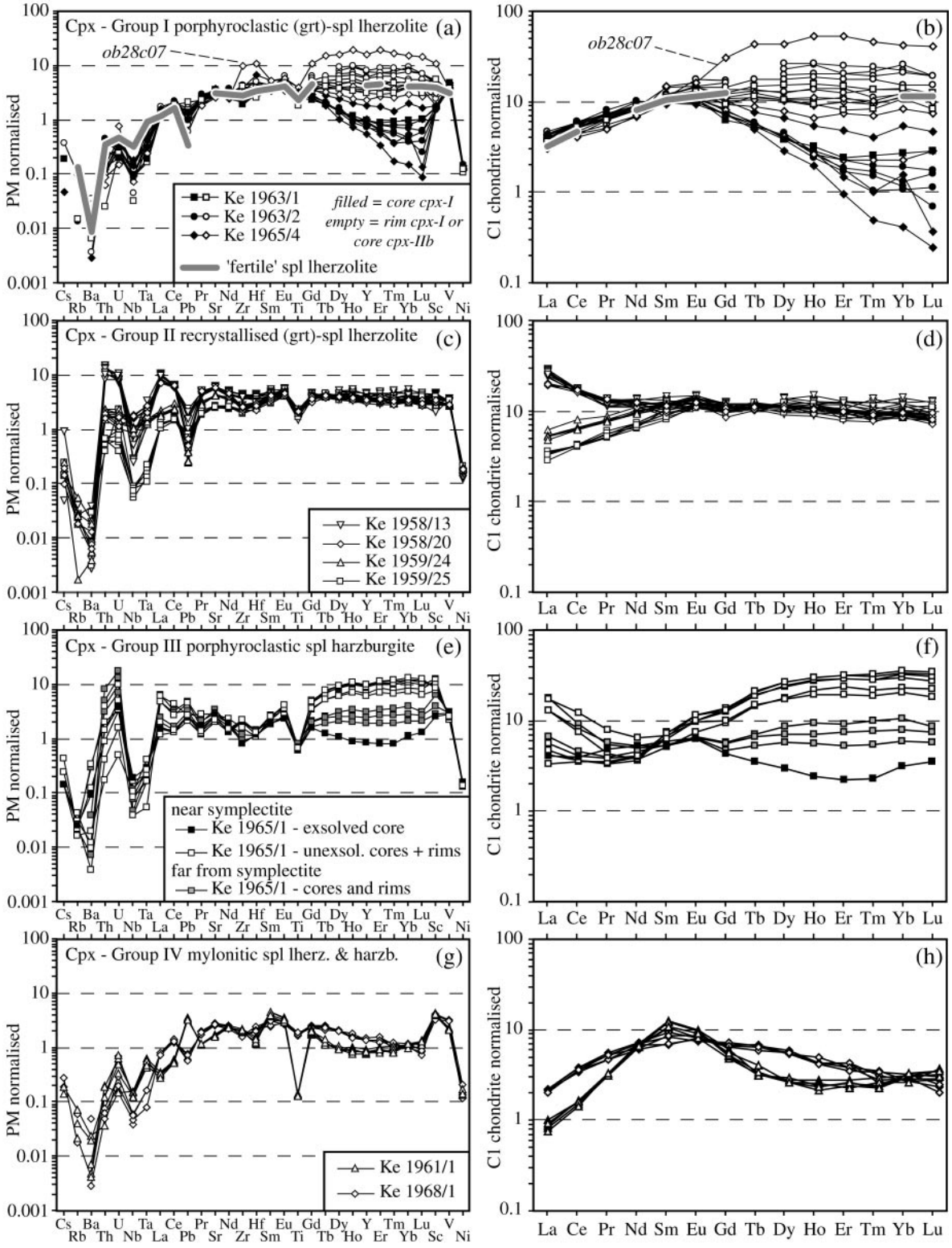

Fig. 7. Trace element characteristics of clinopyroxene in the peridotite xenoliths of Marsabit. (a, b) Group I porphyroclastic (grt)–spl-lherzolite; (c, d) Group II recrystallized (grt)–spl-lherzolite; (e, f) Group III porphyroclastic spl-harzburgite; (g, h) Group IV mylonitic spl-lherzolite and -harzburgite. Fertile spl-lherzolite [grey line in (a)] is taken from Eggins *et al.* (1998). Extended trace element patterns (a, c, e, g) are normalized to primitive mantle; REE patterns (b, d, f, h) are normalized to C1 chondrite [all normalizing values from McDonough & Sun (1995)].

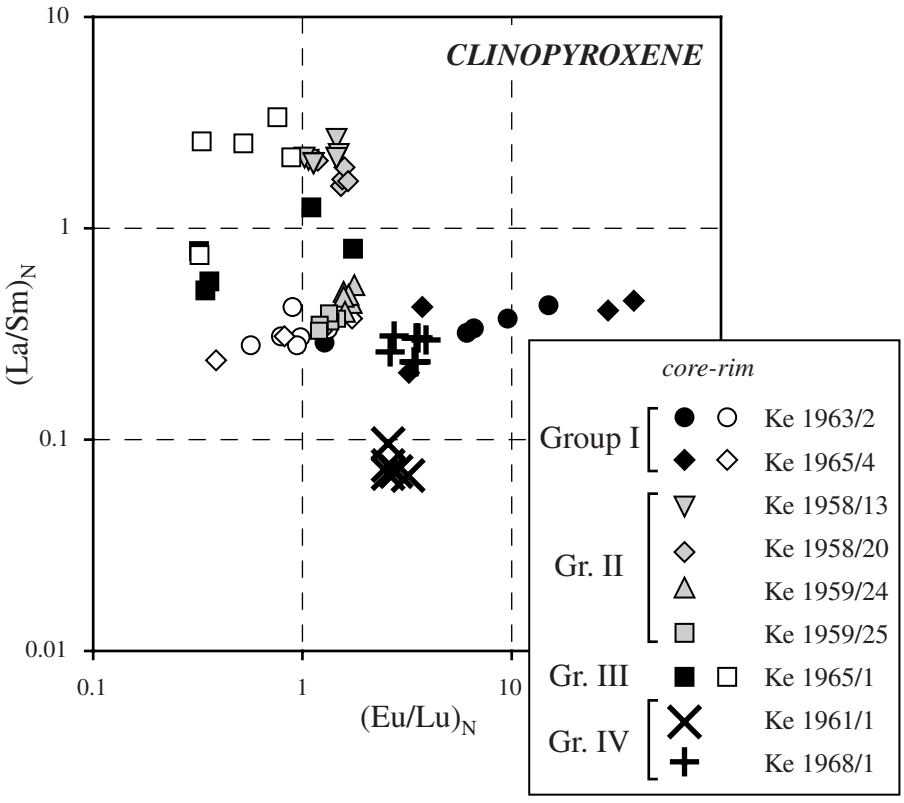

Fig. 8. REE systematics of clinopyroxene in peridotites from Marsabit. $(La/Sm)_N$ and $(Eu/Lu)_N$ are both normalized to C1 chondrite (McDonough & Sun, 1995).

characteristics of the ultramylonite (Ke 1961/1) are different (Fig. 7g and h). REE patterns are sinusoidal, with LREE abundances strongly fractionated from MREE (Fig. 8). Further, clinopyroxene in Ke 1961/1 is extremely depleted in Ti (<170 ppm).

Orthopyroxene

Orthopyroxenes (Fig. 9a–d) from Groups I and II have straight REE patterns with positive slopes from LREE to HREE. Group II orthopyroxenes have slightly higher REE concentrations than those from Group I (Fig. 9b). Orthopyroxenes from Group III (Fig. 9c) show similar patterns. Positive anomalies compared with neighbouring REE are found for Pb, Hf, Zr and Ti, which is a typical feature of orthopyroxene in upper mantle spl-peridotites (Rampone *et al.*, 1991; Eggins *et al.*, 1998). Group IV orthopyroxenes are characterized by lower REE abundances as observed in the associated clinopyroxene (Fig. 9d). Orthopyroxene from Ke 1961/1 (ultramylonite) lacks the positive Ti spike (Fig. 9d).

Ti-pargasite and phlogopite

Ti-pargasites from Group I (grt)–spl-lherzolite have depleted LREE patterns (Fig. 10a). Other characteristics are positive anomalies for Nb [with $(Nb/Ta)_N = 1{\cdot}76$–$3{\cdot}15$], Sr and Ti, and very strong negative U and Th anomalies. The MREE to HREE contents are similar to those of clinopyroxene in Group I, with amph-i tending towards lower HREE contents than amph-ii and -iii. Further, K-rich amph-i has higher large ion lithophile element (LILE; e.g. Rb, Ba), as well as Pb abundances (Table 8; Fig. 10a). Group I phlogopite is characterized by very low REE abundances (Fig. 10b). In contrast, it is the major repository for the LILE (Cs, Rb, Ba), and it contains considerable amounts of Nb, Ta, Pb, Sr and Ti (Table 8; Fig. 10b).

Amphiboles from strongly metasomatized Group III samples are LREE enriched [$(La/Yb)_N$ 2–32; Kaeser *et al.*, in preparation]. Further, both amphibole and phlogopite are characterized by U–Th enrichment and show marked negative Zr–Hf–Ti anomalies (Kaeser *et al.*, in preparation).

Olivine and spinel

Both olivine and spinel contain incompatible element abundances mostly below the limit of detection (Table 9), with the exception of V, Ni, Zn, Ga and Pb and Nb (spinel).

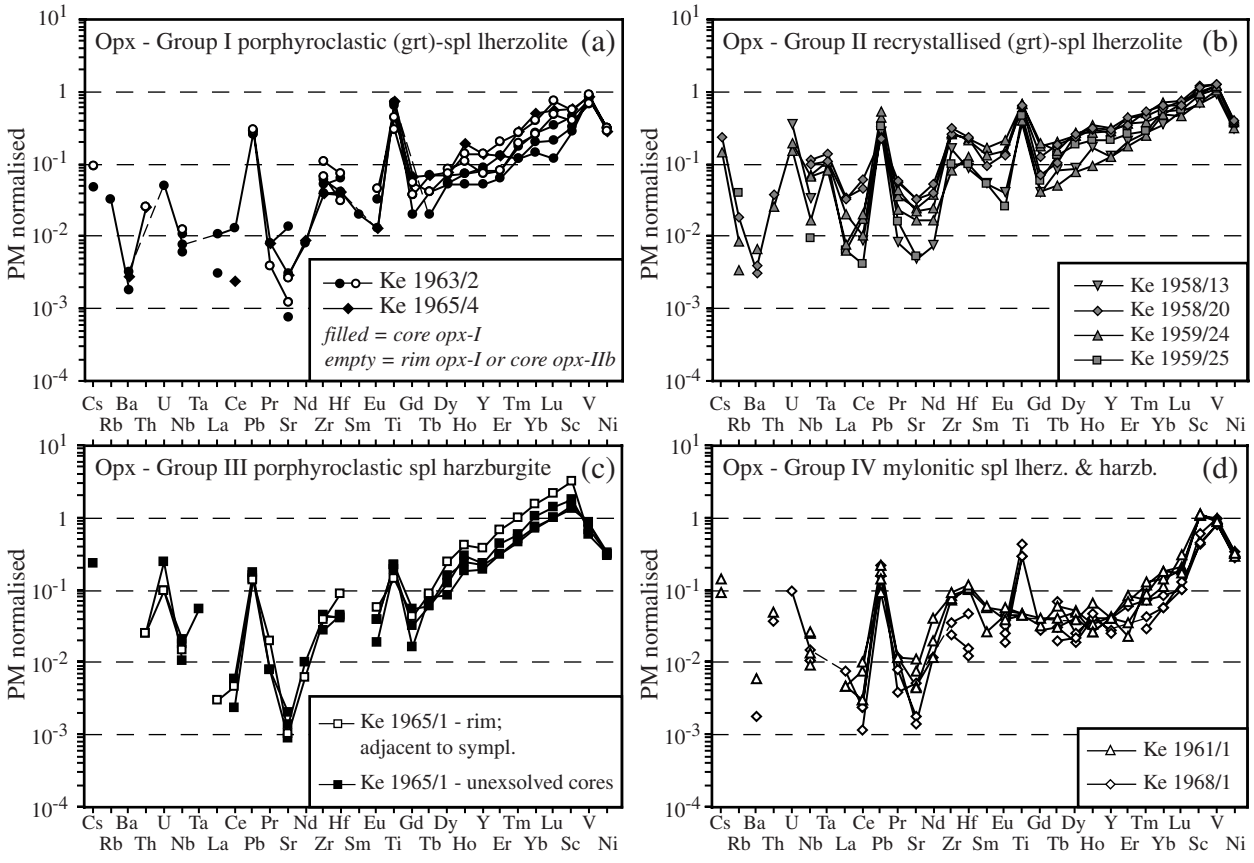

Fig. 9. Trace element characteristics of orthopyroxene in the peridotite xenoliths of Marsabit. (a) Group I porphyroclastic (grt)–spl-lherzolite; (b) Group II recrystallized (grt)–spl-lherzolite; (c) Group III porphyroclastic spl-harzburgite; (d) Group IV mylonitic spl-lherzolite and -harzburgite [values normalized to the primitive mantle values of McDonough & Sun (1995)].

SYNTHETIC SUMMARY OF TEXTURES AND MINERAL COMPOSITIONS

Porphyroclastic peridotites range in composition from lherzolite (Group I) to harzburgite (Groups III and IV). They are characterized by abundant deformation-related microtextures and considerable compositional variation within single xenoliths (intra-grain and between mineral generations). Textures and compositional features can be interpreted in terms of changing *P–T* conditions, deformation, and variable styles of metasomatism (see discussion below). In Group I rocks, the presence of spl–opx–cpx symplectites, low-Al troughs in the cores of first generation pyroxenes (cpx-I, opx-I), together with exsolution lamellae in the cores of cpx-I are consistent with a decompression and cooling event leading to the transition from a former high-pressure/high-temperature (HP/HT) stage to a medium-temperature (MT) stage (Fig. 11). The formation of symplectites is related to the transition from the garnet- into the spinel-stability field, accompanied by the redistribution of HREE (and Al) from garnet into pyroxenes (increasing concentrations from core to rims; Takazawa *et al.*, 1996; Glaser *et al.*, 1999; Ionov, 2004). Some cpx-I rims yield anomalously high HREE contents (up to ~50 × chondrite; analysis ob28c07 in Table 7 and Fig. 7a and b) that are too high to be in equilibrium with orthopyroxene (apparent $_{Yb}D^{opx/cpx}$ of ~0·02 instead of 0·10–0·20; e.g. Eggins *et al.*, 1998; Bedini & Bodinier, 1999). These rims may be interpreted as selvages overgrown on cpx-I, which inherited the trace element budget of garnet and did not equilibrate with the other peridotite phases [see models proposed by Vannucci *et al.* (1993) for former grt-websterites from Zabargad, and by Takazawa *et al.* (1996) for former grt-lherzolites from the Horoman peridotite].

As spl-harzburgites (Groups III and IV) contained no or only rare garnet, they lack the Al-trough (Figs 5e and 11), and only large cpx-I grains close to symplectites have preserved the low-HREE signature in their cores. The composition of Group I pyroxene neoblasts corresponds to the high-Al bulge in the porphyroclasts of these rocks (Figs 5b and 11), and thus they also

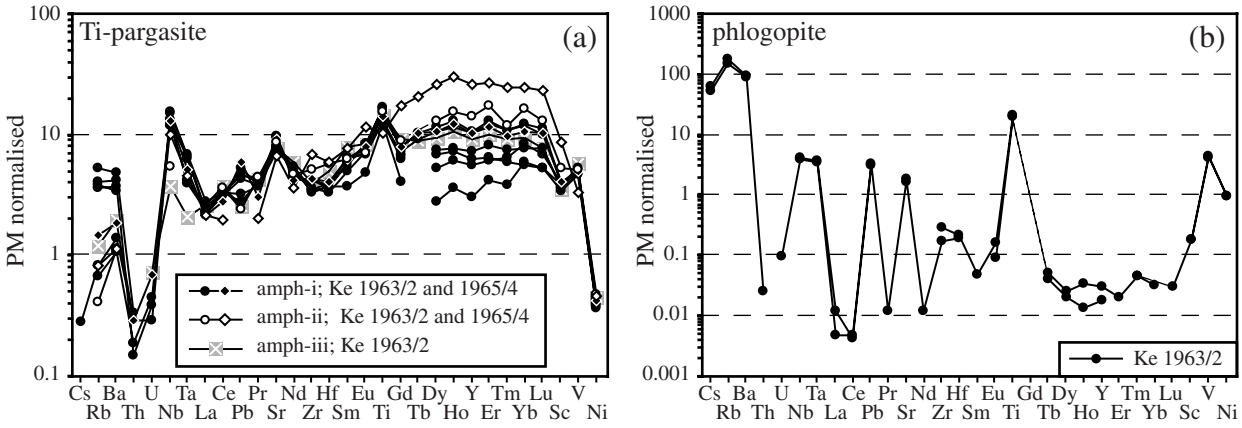

Fig. 10. Trace element characteristics of (a) Ti-pargasite and (b) phlogopite in Group I porphyroclastic (grt)–spl-lherzolite from Marsabit [normalized to the primitive mantle values of McDonough & Sun (1995)].

recorded the MT stage (Fig. 11). Decreasing Al contents towards the rims of both porphyroclasts and neoblasts, observed in all porphyroclastic rock types (Groups I, III and IV), suggest further cooling to a low-temperature stage (MT–LT transition; Fig. 11).

In contrast to the porphyroclastic rocks, mineral grains from strongly recrystallized samples (Group II) are generally homogeneous (Fig. 11), and there is no compositional variation between mineral generations. The mineral compositions in Group II samples range between compositions similar to Group I in less recrystallized samples, towards more 'fertile' compositions in strongly recrystallized samples (lower Mg-numbers in olivine and pyroxenes, higher Al in pyroxenes; Fig. 4a–c). The Al_2O_3–CaO systematics in pyroxenes of strongly recrystallized Group II samples (Fig. 4b and c) is best explained by higher equilibrium temperatures compared with the porphyroclastic rocks (the HT stage; Fig. 11). Concerning the relation of Groups I and II in terms of their *P–T* evolution, two scenarios are possible: (1) Group II was subjected to decompression (i.e. formation of symplectites after garnet) but, in contrast to Group I, remained at constantly higher temperatures, or (2) Group II was subjected to the same *P–T* evolution as Group I (i.e. decompression and cooling during the HT/HP–MT–LT transition), and experienced a later heating event, overprinting the textural and geochemical record of the earlier event. Several textural and compositional characteristics favour the second scenario. These are: (1) bleb-like or elongated orthopyroxene inclusions in some large clinopyroxene grains in strongly recrystallized samples indicating the presence of former exsolution lamellae; (2) zoning patterns for slow-diffusing elements (e.g. Cr and Al, compared with faster diffusing Ca; Sautter *et al.*, 1988) in opx-I from less recrystallized samples indicating cooling (decreasing Cr and Al from core to rim; Fig. 11) followed by heating (rimward increasing Ca; Fig. 11); (3) petrographic similarities on the macroscopic scale between Groups I and II (i.e. high clinopyroxene and garnet contents and layering; Table 1; Fig. 1a and b) indicating a common initial bulk composition.

THERMOBAROMETRY

In the following we present the results of detailed thermobarometric calculations in order to constrain quantitatively the *P–T* evolution during the above stages recorded in the lithospheric mantle beneath Marsabit.

Application of geothermobarometers

A large number of thermometers and barometers have been experimentally and empirically calibrated and extensively tested for upper mantle rocks (Brey & Köhler, 1990; Brey *et al.*, 1990; Werling & Altherr, 1997; Taylor, 1998; Smith, 1999). Thermobarometric calculations in this study were mainly based on the experimentally calibrated thermometers of Brey & Köhler (1990), based on the exchange between enstatite and diopside components in coexisting clino- and orthopyroxene ($T_{2Px\text{-}BK90}$), the Ca content of orthopyroxene in equilibrium with clinopyroxene ($T_{Ca\text{-}opx\text{-}BK90}$), and the partitioning of Na between ortho- and clinopyroxene ($T_{Na\text{-}BK90}$). The barometer based on the Al content in orthopyroxene coexisting with garnet ($P_{Al\text{-}opx\text{-}BK90}$) was applied only to the (grt)-spl-lherzolites of Group I, for which the composition of garnet was recalculated using the bulk composition of its breakdown products (fine-grained symplectites). For other samples, minimum pressures for the appearance of garnet were

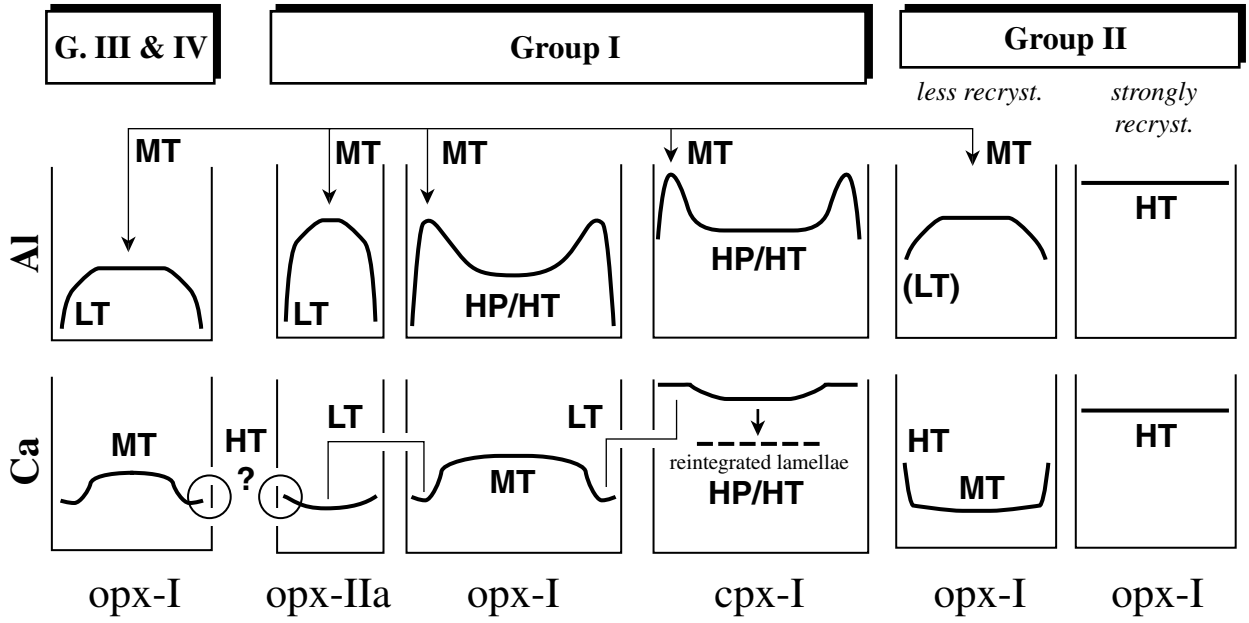

Fig. 11. Interpretation of the observed Al and Ca zoning patterns in pyroxenes of the peridotite xenoliths from Marsabit in terms of changing *P–T* conditions. HP/HT, high-pressure/high-temperature stage; MT, medium-temperature stage; LT, low-temperature stage; HT, high-temperature stage (for further explanation, see text).

calculated using the spinel composition ($P_{\text{grt-in-CWW86}}$; Carroll Webb & Wood, 1986). Further temperature constraints were obtained from the Al and Cr contents of orthopyroxene ($T_{\text{Al,Cr-opx-WS91}}$; Witt-Eickschen & Seck, 1991), the Cr–Al exchange between orthopyroxene and spinel ($T_{\text{opx-spl-SS81}}$; Sachtleben & Seck, 1981), the Fe^{2+}–Mg exchange between olivine and spinel ($T_{\text{ol-spl-B91}}$; Ballhaus *et al.*, 1991), and the partitioning of Cr between clino- and orthopyroxene ($T_{\text{Cr-S99}}$; Seitz *et al.*, 1999). Thermobarometric results are given in Table 10 and a *P–T* compilation is shown in Fig. 12a and b. To be consistent with the reconnaissance study of Henjes-Kunst & Altherr (1992), temperatures for assemblages in the stability field of spinel ('no garnet'; Table 10) were calculated assuming a pressure of 1·2 GPa.

General *P–T* evolution of the samples

Thermobarometric calculations yield 966–1075°C at 2·33–2·87 GPa for the initial HP/HT stage (preserved only by Group I rocks). This was followed by cooling (path 1 in Fig. 12b) to temperatures of around 800–900°C (constrained by Group I, III and IV, as well as less recrystallized Group II xenoliths). Maximum pressures after the breakdown of garnet were <1·5 GPa. The porphyroclastic rocks (Groups I, III and IV) further cooled to very low temperatures (LT; around 750°C). Group II peridotites were later subjected to heating (path 2 in Fig. 12b) resulting in recrystallization and equilibration at high temperatures (HT stage; 1000–1200°C). The two proposed *P–T* paths will be now discussed in detail.

Group I, III and IV xenoliths: decompression and cooling

The *P–T* conditions of the HP/HT stage, prior to pyroxene exsolution and garnet breakdown, were estimated by applying the $P_{\text{Al-opx-BK90}}$ barometer in combination with $T_{\text{2Px-BK90}}$, using the reintegrated composition of clinopyroxene and garnet (Table 6). This yields 966–1075°C at 2·33–2·87 GPa (Table 10). Although Fe/Mg ratios in the recalculated garnet were certainly modified during and after the reaction grt-I + ol-I = spl-IIb + opx-IIb + cpx-IIb, this approach is still justified as the $P_{\text{Al-opx-BK90}}$ barometer does not strongly depend on the garnet composition (Altherr *et al.*, in preparation). We consider $T_{\text{2Px-BK90}}$ based on the reintegrated cpx-I cores to yield relatively accurate results, although the pyroxene's recalculated cores are probably out of equilibrium with respect to Ca. This is shown in Fig. 13, where the Ca content of recalculated opx-I and cpx-I is compared with the experimentally determined equilibrium partitioning at different pressures (Brey *et al.*, 1990). However, the Ca content of a hypothetical orthopyroxene in equilibrium with the recalculated cpx-I (Fig. 13; at 2 GPa similar to that obtained for the HP/HT stage) would yield $T_{\text{Ca-in-opx-BK90}}$ of ~1000–1100°C. This is in good agreement with the above results (966–1075°C)

Table 10: Results of P–T *calculations for peridotite xenoliths from Marsabit (*P *in GPa,* T *in°C)*

	Garnet stability field	No garnet (temperatures at $P_{assumed}$ = 1·20 GPa)							
	$T_{2Px\text{-}BK90}/P_{Al\text{-}opx\text{-}BK90}$	$P_{grt\text{-}in\text{-}CWW86}$	$T_{2Px\text{-}BK90}$	$T_{Ca\text{-}opx\text{-}BK90}$	$T_{Na\text{-}px\text{-}BK90}$	$T_{Cr\text{-}S99}$	$T_{opx\text{-}spl\text{-}SS82}$	$T_{Al,Cr\text{-}opx\text{-}WS91}$	$T_{ol\text{-}spl\text{-}B91}$
Group I: porphyroclastic (grt)-spl-lherz.		(at T = 850°C)							
Ke 1960/2									
cores (recalculated cpx-I, opx-I and grt)	1020 ± 14/2·54 ± 0·12	–	–	–	–	–	–	–	–
Al bulge in opx-I; core in opx-IIa and spl-IIb	–	<1·51	–	897 ± 12	–	–	–	908 ± 21	–
pyroxene and ol-I rims and spl-IIb	–	<1·51	701 ± 40	798 ± 16	711 ± 130	–	705 ± 58	–	811 ± 81
Ke 1963/2									
cores (recalculated cpx-I, opx-I and grt)	1004 ± 38/2·44 ± 0·11	–	–	–	–	–	–	–	–
Al bulge in opx-I; core in opx-IIa and spl-IIb	–	<1·47	–	854 ± 35	–	–	–	850 ± 12	–
pyroxene rims and spl-IIb	–	<1·47	787 ± 38	799 ± 25	746 ± 41	–	–	792 ± 32	–
Ke 1965/4									
cores (recalculated cpx-I, opx-I and grt)	1048 ± 27/2·76 ± 0·11	–	–	–	–	–	–	–	–
Al bulge in opx-I; core in opx-IIa and spl-IIb	–	<1·51	–	869 ± 13	–	–	–	844 ± 17	–
pyroxene and ol-I rims and spl-IIb	–	<1·51	719 ± 38	722 ± 38	716 ± 121	–	658 ± 8	774 ± 54	1011 ± 42
Group II: recrystallized (grt)-spl-lherz.									
Ke 1958/6 (strongly recrystallized)									
cores	–	<1·66	1167 ± 59	1097 ± 8	1205 ± 49	1139 ± 92	–	1032 ± 21	–
rims	–	<1·67	1247 ± 48	1180 ± 27	1270 ± 25	1176 ± 41	–	1048 ± 23	–
Ke 1958/13 (less recrystallized)									
cores	–	<1·66	884 ± 35	855 ± 33	925 ± 42	841 ± 12	862 ± 33	892 ± 28	–
rims	–	<1·66	992 ± 21	908 ± 40	1002 ± 31	876 ± 84	–	853 ± 19	–
Ke 1958/20 (strongly recrystallized)									
cores	–	<1·63	1119 ± 9	1113 ± 9	1121 ± 32	888 ± 50	1072 ± 18	1000 ± 9	–
rims	–	<1·63	1109 ± 11	1068 ± 20	1127 ± 30	1100 ± 56	–	1031 ± 37	–
Ke 1959/24 (strongly recrystallized)									
cores	–	<1·69	1103 ± 11	1053 ± 8	1119 ± 32	1052 ± 78	1037 ± 19	1019 ± 15	–
rims	–	<1·69	1125 ± 10	1077 ± 15	1143 ± 38	1094 ± 54	–	1028 ± 14	–
Ke 1959/25 (less recrystallized)									
cores	–	<1·74	994 ± 13	962 ± 15	1143 ± 38	854 ± 146	–	921 ± 34	–
rims	–	<1·74	1103 ± 99	1031 ± 66	1141 ± 78	991 ± 145	–	930 ± 20	–
Group III: porphyroclastic spl-harzburgite									
Ke 781/6									
cores (and spl-I)	–	<1·69	822 ± 17	866 ± 16	839 ± 65	866 ± 88	863 ± 29	900 ± 30	–
rims (and spl-I)	–	<1·69	859 ± 15	907 ± 9	903 ± 111	986 ± 123	855 ± 27	910 ± 41	1331 ± 107
Ke 1965/1									
cores (and spl-I)	–	<1·93	809 ± 51	864 ± 25	812 ± 131	859 ± 84	756 ± 56	894 ± 27	940 ± 60
rims (and spl-IIb)	–	<1·62	834 ± 32	834 ± 37	895 ± 61	763 ± 121	–	804 ± 47	1092 ± 55
Ke 1965/15 (modally metasomatized)									
cores (no spl-I preserved)	–	–	–	837 ± 46	–	–	–	913 ± 51	–
Group IV: mylonitic spl-lherz. and -harzb.									
Ke 1961/1 (ultramylonitic spl-harzburgite)									
cores (opx-I, cpx-I, ol-I and spl-I)	–	<1·83	834 ± 9	913 ± 18	811 ± 35	950 ± 51	761 ± 25	933 ± 11	792 ± 35
rims (opx-I, cpx-I, ol-I and spl-I), and opx-IIa cores	–	<1·64	–	762 ± 70	804 ± 241	–	–	782 ± 101	1119 ± 85
Ke 1968/1 (mylonitic spl-lherzolite)									
cores (opx-I, cpx-I, ol-I and spl-I)	–	<1·70	722 ± 56	797 ± 32	764 ± 103	791 ± 154	–	848 ± 85	964 ± 58
rims	–	<1·56	711 ± 62	768 ± 21	725 ± 54	703 ± 147	–	770 ± 46	1381 ± 91

Errors are 1σ; for references with respect to thermometers and barometers see text.

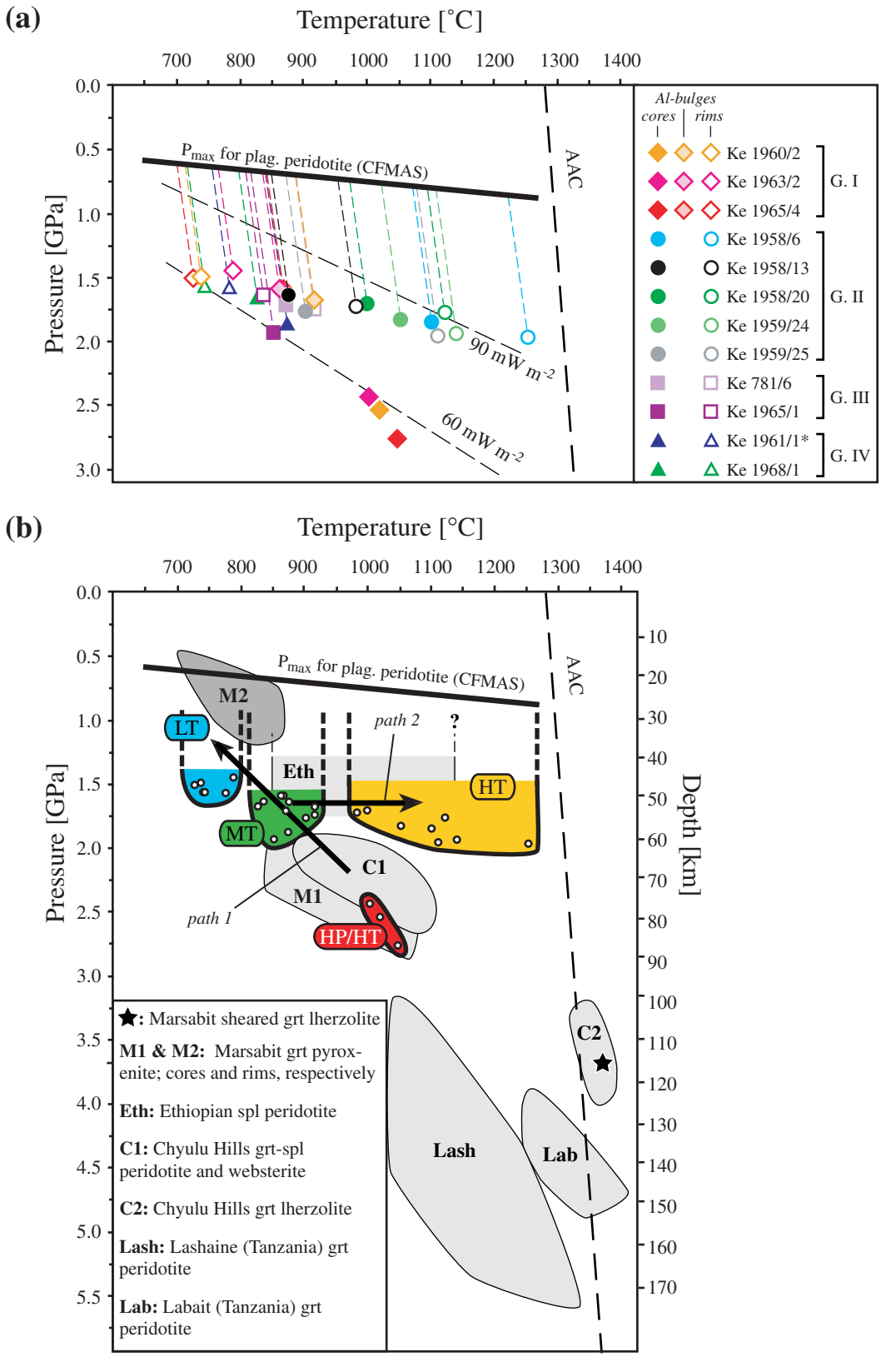
(a)
Temperature [°C]
700 800 900 1000 1100 1200 1300 1400
Pressure [GPa]
0.0 0.5 1.0 1.5 2.0 2.5 3.0
Pmax for plag. peridotite (CFMAS)
AAC
90 mW m-2
60 mW m-2
Al-bulges
cores rims
Ke 1960/2
Ke 1963/2
Ke 1965/4
G. I
Ke 1958/6
Ke 1958/13
Ke 1958/20
Ke 1959/24
Ke 1959/25
G. II
Ke 781/6
Ke 1965/1
G. III
Ke 1961/1*
Ke 1968/1
G. IV
(b)
Temperature [°C]
700 800 900 1000 1100 1200 1300 1400
Pressure [GPa]
0.0 0.5 1.0 1.5 2.0 2.5 3.0 3.5 4.0 4.5 5.0 5.5
Depth [km]
10 20 30 40 50 60 70 80 90 100 110 120 130 140 150 160 170
Pmax for plag. peridotite (CFMAS)
AAC
M2
LT
path 2
?
Eth
HT
MT
C1
M1
path 1
HP/HT
C2
Lash
Lab
★: Marsabit sheared grt lherzolite
M1 & M2: Marsabit grt pyroxenite; cores and rims, respectively
Eth: Ethiopian spl peridotite
C1: Chyulu Hills grt-spl peridotite and websterite
C2: Chyulu Hills grt lherzolite
Lash: Lashaine (Tanzania) grt peridotite
Lab: Labait (Tanzania) grt peridotite

and shows that $T_{2Px\text{-}BK90}$ depends mostly on the Ca content in the clinopyroxene.

Temperatures from $T_{Ca\text{-}opx\text{-}BK90}$ using the measured Ca contents in the cores of Group I opx-I are consistently lower (819–909°C) than those based on two-pyroxene thermometry. Similar temperatures (differing by less than ~25°C within each sample) are obtained by $T_{Al,Cr\text{-}opx\text{-}WS91}$, based on the Al and Cr contents of the high-Al bulge of opx-I and of the cores of opx-IIa neoblasts (827–929°C; Table 10). Therefore, we interpret the Ca plateau in opx-I (Fig. 5a) to reflect re-equilibration during the MT stage (Figs 11 and 12b), i.e. the *P–T* conditions after cooling and decompression. The fact that the Al and Ca contents in the opx-I cores represent different *P–T* stages may be explained by the faster diffusion of Ca in pyroxenes compared with Al or Cr (Sautter *et al.*, 1988; Witt-Eickschen & Seck, 1991). Temperature estimates based on the core composition of the neoblasts (opx-IIa and cpx-IIa) give the same temperature range (MT stage), in agreement with the hypothesis that deformation and recrystallization occurred after and/or during the HP/HT–MT transition.

The MT stage is, in addition to Group I rocks, also recorded in Group III and IV spl-peridotites (e.g. the high Al and Ca plateaux in Group III opx-I; Figs 5e and 11). Thermometers applied to the core composition of opx-I, cpx-I, ol-I and spl-I of most Group III and IV samples yield temperatures between 750 and 900°C (Table 10). As cpx-I in Group III generally lacks exsolution lamellae, no information on an eventual higher temperature stage can be obtained. Indications for a former equilibrium at higher pressures can, however, be inferred in Group III samples from the presence of rare symplectites, and from the low HREE contents in some large cpx-I porphyroclasts (e.g. xenolith Ke 1965/1; Fig. 7f). This indicates a similar *P–T* evolution of Group I and III samples (i.e. transition from HP/HT to MT).

In addition, all pyroxenes from Groups I, III and IV indicate further cooling to an LT stage, as shown by decreasing Al contents towards the rims (Figs 5, 6 and 11). This is supported by lower Ca contents in the rims of large opx-I porphyroclasts (both Groups I and III; Fig. 5a and e). The ultramylonitic Group IV sample (Ke 1961/1) lacks zoning but cpx-I contains abundant spinel and orthopyroxene lamellae, also indicating cooling. The degree of cooling may be quantified with the $T_{Al,Cr\text{-}opx\text{-}WS91}$ thermometer. From the Al bulges to the rims in Group I (Ke 1963/2, Ke 1965/4), and from cores to rims in Group III, respectively (Ke 1965/1), a temperature decrease of ~60–90°C has been calculated (Table 10; Fig. 12b). Rim temperatures obtained with $T_{2Px\text{-}BK90}$, $T_{Ca\text{-}opx\text{-}BK90}$ and $T_{Na\text{-}px\text{-}BK90}$ (at an assumed pressure of 1·20 GPa) are mostly <850°C, reaching very low values around 750°C (Table 10). In Group I, comparison between results from mineral pairs within (not shown) and outside symplectites revealed no significant differences. In the ultramylonite (Ke 1961/1: Group IV), neoblast cores (opx-IIa) also record very low temperatures (Table 10), indicating that the mylonitization occurred during the MT–LT transition. Generally, temperatures below ~850°C must be regarded with caution because of low diffusion rates and proximity to the closure temperature for the diopside–enstatite exchange reaction (e.g. Smith, 1999). However, the results are in fairly good agreement with temperatures obtained by $T_{opx\text{-}spl\text{-}SS81}$ and $T_{Cr,Al\text{-}opx\text{-}WS91}$ (Table 10). In some samples, calculations using rim compositions and fast reacting thermometers, i.e. based on fast diffusing elements (Mg–Fe in spinel and olivine in the case of $T_{ol\text{-}spl\text{-}B91}$; Chakraborty *et al.*, 1994), result in considerably higher temperatures (1000–1300°C; Table 10). They are interpreted either to be related to the same heating event as recognized in the Group II peridotites (the HT event; Fig. 11), or to reflect heating by the host basanite during the transport of the xenolith to the surface.

All temperatures calculated for the MT and LT stages correspond to an assumed pressure of 1·2 GPa (Table 10) and are projected to maximum pressures based on the Cr content of associated spinel (Fig. 12a and b). The maximum pressure for the MT stage after the breakdown of garnet is <1·51 GPa (Table 10), defined by the Cr content of symplectitic spinel of Group I xenoliths (spl-IIb). Similarly low maximum pressures are indicated by the low-Cr rims in the mylonitic spl-peridotites (Table 2).

Group II xenoliths: heating and recrystallization

Based on textural evidence, it was suggested that the recrystallized Group II lherzolites represent heated, recrystallized and variously metasomatized equivalents of formerly deformed Group I lherzolites. These

Fig. 12. *P–T* estimates for peridotite xenoliths from Marsabit. (a) *P–T* conditions calculated for each sample based on evaluation of mineral zoning patterns. Dashed subvertical lines indicate that corresponding symbols represent maximum pressures. Minimum pressures are defined by the absence of plagioclase (from Gasparik, 1987). The steady-state model geotherms (long dash lines) are from Pollack & Chapman (1977), the asthenospheric adiabatic upwelling curve (AAC) is from McKenzie & Bickle (1988). (b) Interpretation of our *P–T* estimates and comparison with thermobarometric results from other xenolith suites along the EARS: Marsabit (Henjes-Kunst & Altherr, 1992; Olker, 2001), Ethiopia (Bedini *et al.*, 1997), Chyulu Hills (Altherr *et al.*, in preparation), Lashaine and Labait (Lee & Rudnick, 1999). *P–T* path 1 describes decompression and cooling from an initial high-*P*/high-*T* stage (HP/HT), via a medium-*T* stage (MT) to a low-*T* stage (LT). Group II xenoliths experienced later heating from MT to HT described as *P–T* path 2 (for further explanation, see text).

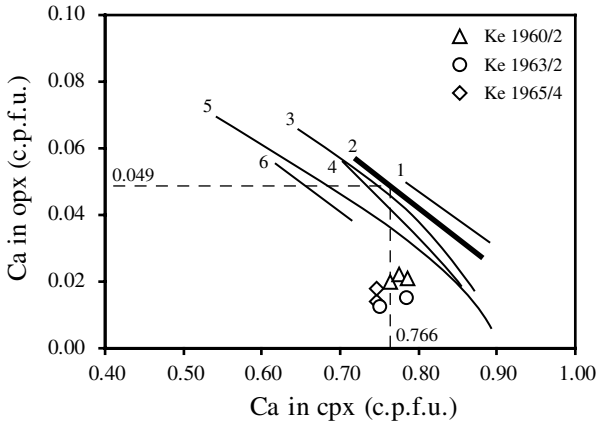

Fig. 13. Ca_{cpx} vs Ca_{opx} (cations per formula unit; c.p.f.u.) for reintegrated cpx-I and opx-I from Group I porphyroclastic (grt)–spl-lherzolite. Comparison with the experimental results of Brey *et al.* (1990) indicates that the reintegrated cores of cpx-I and opx-I are not in equilibrium with respect to Ca (lines labelled 1–6 represent equilibrium partitioning at 1–6 GPa). Assuming a pressure of 2·0 GPa, the mean Ca content in cpx would be in equilibrium with an opx with about 0·049 Ca p.f.u. (dashed lines), corresponding to temperatures of about 1000–1100°C (applying $T_{Ca\text{-}opx\text{-}BK90}$; Brey & Köhler, 1990; for discussion see text).

assumptions are supported by zoning patterns (Fig. 11) and thermobarometric calculations (Table 10). Temperatures based on the core composition of minerals from less recrystallized samples (Ke 1958/13 and Ke 1959/25) using slowly reacting thermometers (based on Al and Cr; $T_{Cr\text{-}S99}$, $T_{opx\text{-}spl\text{-}SS82}$, $T_{Al,Cr\text{-}opx\text{-}WS91}$) give similar values (~840–960) to those found for the MT stage in the porphyroclastic rocks (Table 10; Fig. 12a). In contrast, temperatures using rim compositions and thermometers based on faster diffusing elements ($T_{2Px\text{-}BK90}$, $T_{Ca\text{-}opx\text{-}BK90}$, $T_{Na\text{-}px\text{-}BK90}$) yield higher temperatures (Table 10; Fig. 12a). This may produce apparently contradictory zoning patterns in some opx-I from less recrystallized Group II xenoliths (Fig. 5c): the initial cooling event (MT–LT transition) is still preserved by the more slowly diffusing Al, whereas the subsequent heating is indicated by a rimward increase of the faster diffusing Ca.

The homogeneous mineral compositions in the strongly recrystallized samples can be explained by almost complete equilibration at the HT stage. This is supported by temperature calculations, which yield consistently high values for both cores and rims, and for all applied thermometers (around 1000–1200°C at 1·20 GPa; Table 10). The only exception is $T_{Cr\text{-}SS99}$, which records the MT stage also in one strongly recrystallized sample (Ke 1958/20; Table 10).

The recalculated bulk compositions of symplectites or clusters in Group II samples do not satisfy a garnet stoichiometry; this result is probably due to recrystallization and equilibration at higher temperatures (Morishita & Arai, 2003). Therefore, we calculated only maximum pressures from spinel compositions ($P_{grt\text{-}in\text{-}CWW86}$) of 1·63–1·74 GPa (Table 10; Fig. 12a)

GEOCHEMICAL AND TEXTURAL EVOLUTION OF THE LITHOSPHERIC MANTLE BENEATH MARSABIT

The Marsabit mantle xenoliths reflect the thermal and compositional state of the lithospheric mantle at maximum depths of ~45–60 km at the time of sampling by their host lava. In addition, older episodes of (partial) chemical and P–T equilibration are recorded in the samples to different degrees. In this section we combine P–T stages (Figs 11 and 12) with textures and geochemical signatures, to constrain the relative timing of deformation and metasomatism in the lithospheric mantle beneath this part of the EARS (Fig. 14). The details outlined below can be summarized as follows: penetrative deformation observed in all porphyroclastic peridotites is related to decompression and cooling from the initial HP/HT stage, representing the oldest preserved feature, to the MT stage. This was accompanied by subsolidus redistribution of major and trace elements in the context of the transition from garnet to spinel stability. In addition, the penetrative deformation accounts for the generally very fertile character of some xenolith types (Group I), as they probably represent the result of mechanical addition of pyroxenitic material to the peridotitic mantle. Finally, metasomatism in Group II and III xenoliths, as well as heating and recrystallization in Group II xenoliths, is related to the younger HT stage (subsequent to the MT stage).

Porphyroclastic xenoliths

Group I rocks have anomalous modal compositions (Table 1). Their high clinopyroxene and initial garnet contents make them too fertile to represent an ancient melting residue and even conflict with their classification as mantle peridotites. Calculated bulk-rock compositions (not shown) yield up to 6 wt % Al_2O_3, which is considerably higher than primitive mantle estimates (McDonough & Sun, 1995). Other compositional parameters, such as the Mg-numbers of olivine (Table 2), on the other hand, are consistent with fertile lherzolite (89–90; e.g. Pearson *et al.*, 2003). These apparently contradictory features may be explained by metasomatic addition of clinopyroxene and garnet (refertilization), as observed in some cratonic xenoliths (Simon *et al.*, 2003). The lack of enriched trace element patterns in Group I clinopyroxene (Fig. 7b), however,

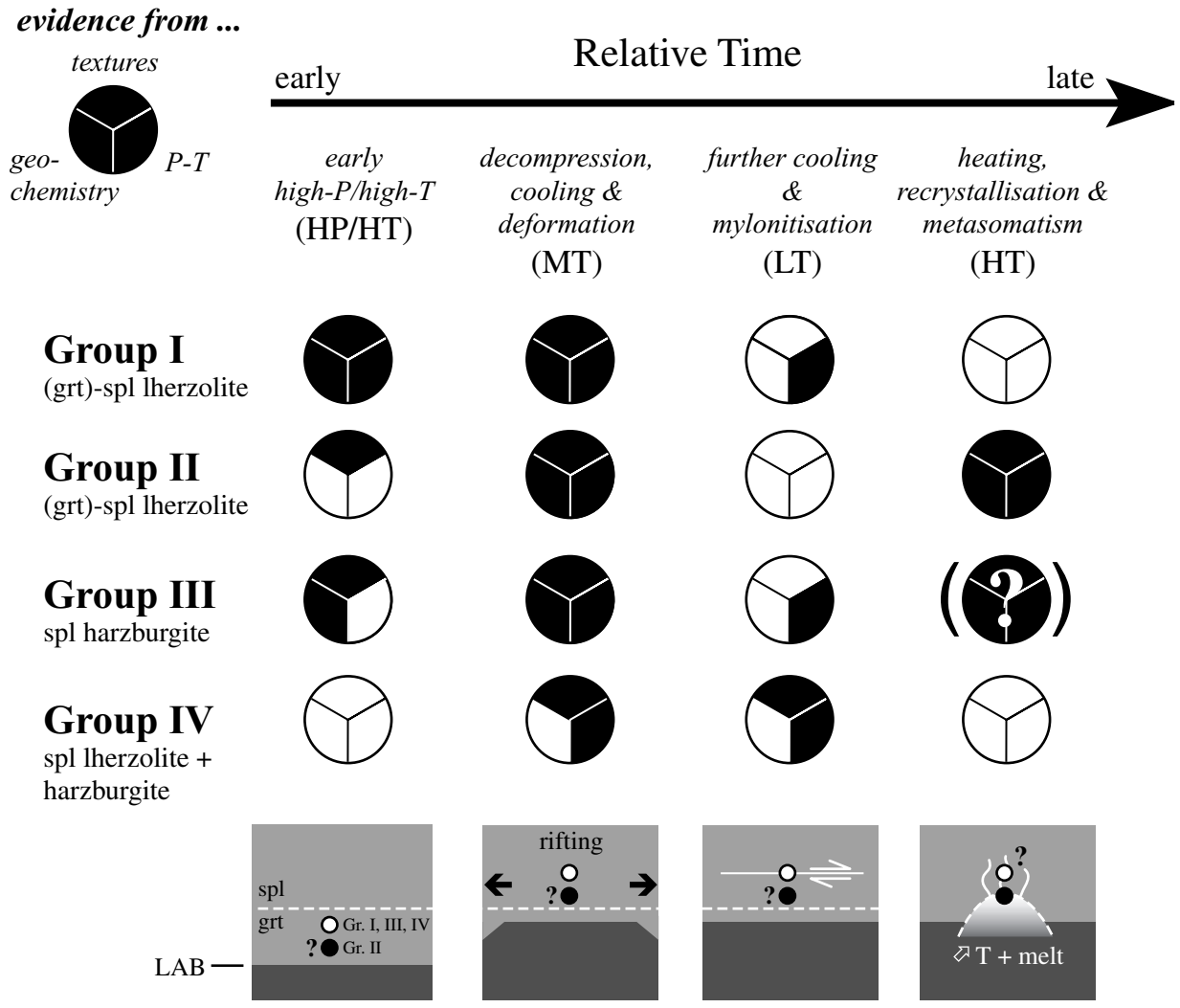

Fig. 14. Schematic representation of the relative timing of events recorded by the Marsabit peridotite xenoliths. Filled sectors of circles denote which events are recorded by a given xenolith type and by which type of evidence (textures, thermobarometry, trace element geochemistry). Block diagrams at the bottom represent simplified cross-sections through the lithospheric mantle and the upper asthenosphere (LAB, lithosphere–asthenosphere boundary) and present a simplified model of lithospheric evolution through time. No absolute timescale can be attributed because of the lack of accurate dating methods (for discussion see text).

argues against this hypothesis. The fact that all of the investigated Group I samples are pervasively deformed is more in favour of a model of mechanical, solid-state mingling of peridotite and pyroxenite (e.g. Bodinier *et al.*, 1988). The result will be heterogeneous zones consisting of more and less pyroxene-rich peridotites or olivine websterites. This is observed in some Group I xenoliths (layering; Fig. 2a). Similar models, based on petrographic observations, have been proposed in some cases for the peridotite–grt-pyroxenite relationship in orogenic peridotite massifs, such as Lherz (Bodinier *et al.*, 1988), Beni Bousera (Kornprobst, 1966; Tabit *et al.*, 1997), Ronda (Schubert, 1977; van der Wal & Vissers, 1996) and Malenco (Müntener & Hermann, 1996). Although garnet websterites form an important part of the Marsabit xenolith suite, no composite xenoliths were found and no trace element data on the pyroxenite xenoliths are yet available, which would allow us to further constrain the peridotite–pyroxenite relationship. However, a spatial relationship in the mantle with the porphyroclastic peridotites is supported by thermobarometry, i.e. the P–T evolution obtained for the Group I lherzolites is in good agreement with thermobarometric studies on these pyroxenites (cooling and decompression from 1066–926°C at 2·51–1·41 GPa to 859–712°C at 1·15–0·75 GPa; Henjes-Kunst & Altherr, 1992; Olker, 2001; see fields M1 and M2 in Fig. 12b).

Unfortunately, no data are at present available for characterizing the age and exact nature of the pyroxenitic material. The fact that the clinopyroxene- and (initially) garnet-rich layers are oriented parallel to the foliation indicates that the peridotite–pyroxenite mingling is probably the result of the penetrative deformation event (or older). Deformation, in turn, is associated with the MT stage (Fig. 14), as indicated by textural and compositional features in the Group I rocks (i.e. zoning, *P–T* conditions and high HREE abundances recorded by neoblast cores, as well as bent exsolution lamellae in cpx-I). It is worth noting that the HP/HT and MT stages are also manifested in some Group III and IV peridotites, indicating a close spatial relationship between all porphyroclastic peridotite types.

In addition to deformation, the porphyroclastic rocks show a metasomatic overprint, which is different in Group I and Group III. All Group I Ti-pargasites have constant and mostly depleted incompatible trace element abundances (e.g. LREE, U, Th; Fig. 10a), whereas the HREE show strong variation between the cores of K- and LILE-rich amph-i grains and texturally 'younger' amph-ii and -iii (Fig. 10a). The REE signature of amph-i, together with the LREE-depleted nature of the associated clinopyroxenes, suggests that K-rich Ti-pargasite (+ phlogopite) represents an 'old' modal metasomatic assemblage that re-equilibrated with the surrounding mineral matrix. This resulted in depleted LREE and low HREE, in equilibrium with associated clinopyroxene and garnet (Vannucci *et al.*, 1995). Similar Mg-numbers of amphibole and silicates (olivine) further support this idea. Equilibrium with garnet (low HREE) indicates an age related to the HP/HT stage. The temperature estimates for the HP/HT stage (Fig. 12b) are consistent with the experimentally determined stability of Ti-pargasite under upper mantle conditions (1075°C between 1·8 and 2·5 GPa: Niida & Green, 1999). It is most probable that amph-i and phlogopite belong to the pyroxenite component that was introduced mechanically in the peridotite. This is indicated by almost identical compositions of Ti-pargasites and phlogopite in the grt-websterites (Olker, 2001). This would also explain the confinement of Ti-pargasite to the clinopyroxene-rich Group I rocks. The high-HREE Ti-pargasite (amph-ii and -iii) probably represents secondary amphibole resulting from subsolidus recrystallization of primary amph-i during decompression. Re-equilibration with spinel led to HREE-rich, but still LREE-depleted compositions.

The presence of cold mylonites (Group IV) further testifies to zones of strongly focused strain in the shallow lithospheric mantle, probably associated with the MT–LT transition (Fig. 14). Deep-seated shear zones near the asthenosphere–lithosphere boundary (field 'C2' in Fig. 12b) are documented by sheared garnet-bearing lherzolites from the Chyulu Hills, as well as from Marsabit (star in Fig. 12b; Henjes-Kunst & Altherr, 1992). Along with the cold, shallow-level, sheared Group IV peridotites from this study, they indicate shear zones at different levels in the lithospheric mantle beneath Marsabit.

Apart from low sulfide contents in Ke 1961/1, the two mylonitic samples show no evidence for metasomatism. The conspicuous trace element signature of cpx-I in the ultramylonitic spl-harzburgite (sinusoid REE pattern and extreme Ti depletion; Fig. 7g and h) is difficult to explain. The strongly depleted incompatible trace elements, however, seem to preclude a metasomatic event.

In contrast to Groups I and IV, spl-harzburgites of Group III are characterized by variable enrichment in incompatible elements (Figs 7e and 8), providing evidence of a different metasomatic event compared with Group I. Detailed descriptions and chemical data will be given in a forthcoming paper (Kaeser *et al.*, in preparation). Metasomatism ranges from cryptic (enrichment of clinopyroxene; Figs 7e and f, and 8) to modal, the latter resulting in the crystallization of amphibole, phlogopite, apatite and graphite. Metasomatism led to enrichment of LREE, Th and U, whereas Hf, Zr and Ti show negative anomalies (Fig. 7e and f). The amphibole and phlogopite compositions point to a Si–Na-rich and relatively Ca-poor metasomatic agent. This, along with the fact that orthopyroxene is a stable phase in the metasomatic assemblages whereas clinopyroxene is not, argues in favour of a Si-rich, orthopyroxene-saturated fluid or melt, and against a carbonatitic melt. Absence of deformation in the modal metasomatic assemblages, as well as replacement textures indicate that metasomatism post-dates the penetrative deformation. Compositional similarities with respect to the trace element signatures in some Group II xenoliths imply that metasomatism in Groups II and III was possibly related to the same, relatively late event (see Fig. 14 and discussion below).

Recrystallized xenoliths—cryptic metasomatism

Group II xenoliths provide evidence of the same early *P–T* evolution as Group I (transition from the HP/HT to the MT stage), which was followed by heating to the HT stage (Figs 12b and 14). Importantly, they also contain initial pyroxene-rich layers (Fig. 1b); this feature suggests that they were subjected to the same deformation-related pyroxenite–peridotite mingling as Group I xenoliths (MT stage). Because of the lack of absolute depth constraints (only maximum pressures), we have no information on whether Group II xenoliths originated at greater depths than Group I samples, or if they reflect lateral temperature heterogeneities

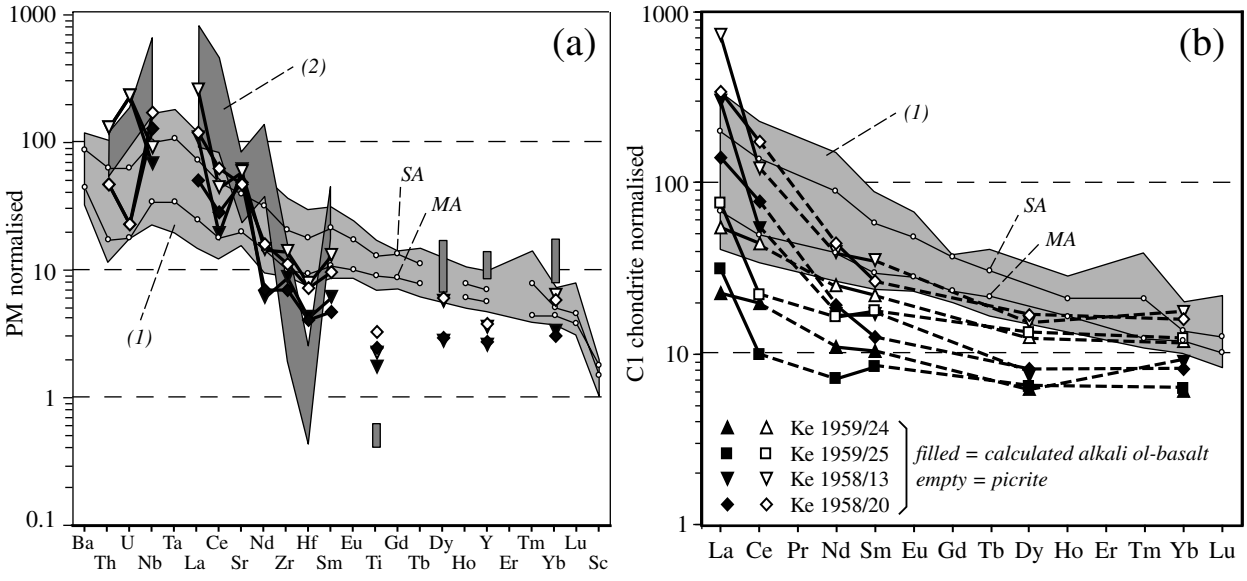

Fig. 15. Primitive mantle normalized (a) and chondrite-normalized (b) trace element patterns of calculated melts in equilibrium with Group II (grt)–spl-lherzolite xenoliths from Marsabit [normalizing values from McDonough & Sun (1995)]. Clinopyroxene/melt partition coefficients for picritic and alkali ol-basaltic melts are from Skulski *et al.* (1994; their runs TS137 and TS139, respectively). Partition coefficients for U and Th are from Wood *et al.* (1999). SA and MA are average of strongly and mildly alkaline Quaternary basanites and alkali basalts, respectively, from Marsabit (Volker, 1990); (1) compositional range of Quaternary basanites and alkali basalts from Marsabit (Volker, 1990); (2) range of calculated silicate melts in equilibrium with amphibole-rich harzburgites (Group III) from Marsabit (see Kaeser *et al.*, in preparation).

(e.g. proximity to magma intrusions or conduits; note that the deeper position of Group II indicated in Fig. 14 is schematic and purely hypothetical).

In addition to heating, Group II samples show evidence of cryptic metasomatism (enriched clinopyroxene trace element patterns; Fig. 7c and d). There is a relationship between the degree of recrystallization, equilibration temperatures and metasomatism: being texturally closest to Group I xenoliths, sample Ke 1959/25 shows clinopyroxene trace element patterns almost identical to those of Group I clinopyroxene after the breakdown of garnet (Fig. 5c and d). From Ke 1959/24 to Ke 1958/20, there is a progressive enrichment in LREE, U and Th. The most enriched signature in these elements is developed in clinopyroxene from the sample with the most pronounced foliation (Ke 1958/13; Fig. 5c and d). Thus, the metasomatizing agent seems to be focused in zones with an anisotropic fabric.

Ti concentrations in clinopyroxene (in sample Ke 1958/6; Fig. 4b), and slightly lower Mg-numbers in olivine and pyroxenes in the strongly recrystallized and heated samples indicate Fe–Ti enrichment, consistent with metasomatism and heating by a mafic silicate melt (Menzies *et al.*, 1985; Bodinier *et al.*, 1990, 2004). This is further supported by the more ferric and Ti-enriched composition of Group II spinel (Table 1; Dick & Bullen, 1984; Xu *et al.*, 1998). In addition, the moderate negative Hf, Zr and Ti anomalies in Group II clinopyroxene (Fig. 7c) are balanced by slightly positive anomalies in the associated orthopyroxene (Fig. 9b). Thus, calculated whole-rock trace element patterns would be devoid of negative anomalies (e.g. Rampone *et al.*, 1991), consistent with metasomatism by mafic melts (e.g. Bodinier *et al.*, 1990).

To constrain the exact nature of the metasomatizing agent responsible for cryptic metasomatism in Group II samples, hypothetical melts in equilibrium with the phase assemblage of each studied Group II xenolith (Table 1) were calculated using published clinopyroxene/melt partition coefficients ($D^{cpx/melt}$; see Fig. 15 for references). Values for $D^{opx/melt}$ and $D^{ol/melt}$ (for calculation of the bulk-rock partition coefficient) were derived from the respective temperature-dependent $D^{cpx/opx}$ and $D^{cpx/ol}$, using the equations of Witt-Eickschen & O'Neill (2005). Melts in equilibrium with samples containing LREE-enriched clinopyroxene (Ke 1958/13 and 1958/20) approach the LREE composition of the strongly alkaline host basanites (SA in Fig. 15). The less incompatible elements (from Sm to Lu), on the other hand, exhibit lower abundances, and do not overlap with the MREE–HREE range shown by the alkali basalts and basanites. Such REE variation is commonly explained by chromatographic trace element fractionation during open-system melt percolation (e.g. Navon & Stolper, 1987). In Fig. 15, extended trace element patterns for hypothetical melts in equilibrium with the

most strongly metasomatized Group II samples are shown. The incompatible element patterns (U, Th, Nb, Ta, LREE and Sr) of the calculated melt in equilibrium with the enriched, strongly heated, completely equilibrated, and strongly recrystallized xenolith (Ke 1958/20) indicate that the metasomatizing agent was probably parental to the Quaternary Marsabit basanites and alkali basalts (Fig. 15). The less heated and recrystallized, slightly foliated, sample (Ke 1958/13) is in equilibrium with a melt with higher abundances of incompatible elements, bearing some similarities to melts in equilibrium with the amphibole-rich harzburgites (Fig. 15 and Kaeser *et al.*, in preparation). This transition from strongly deformed xenoliths with respect to less heated and recrystallized Group II lherzolites, to modally metasomatized Group III harzburgites, indicates that metasomatism in Group II and III samples is probably the result of a single event. The different styles of expression either reflect different agents or are the result of reactive fractionation upon melt percolation depending on different temperatures, melt/rock ratios, phase assemblages, modal proportions, and element diffusivities (Vasseur *et al.*, 1991; Bedini *et al.*, 1997, 2004; Vernières *et al.*, 1997; Ionov *et al.*, 2002; Xu & Bodinier, 2004; Yu *et al.*, 2006; Kaeser *et al.*, in preparation).

GEODYNAMIC IMPLICATIONS

Calculated melts in equilibrium with the heated and recrystallized Group II xenoliths (Fig. 15) indicate that the young (HT-related) metasomatic event was probably related to the Tertiary to Quaternary magmatic activity in Marsabit. Consequently, the HT event was probably part of EARS-related processes. The late heating and melt infiltration (HT stage) produced geochemical signatures similar to those observed in xenoliths from Mega, southern Ethiopia (U–Th–LILE–LREE enrichment; Bedini *et al.*, 1997), which have been modelled in the context of Tertiary, EARS-related thermomechanical erosion of the lower lithosphere atop hotter material (e.g. a mantle plume).

For Marsabit, the integration of thermobarometry, compositional data and textures provides evidence that the late heating and melt infiltration (HT stage) postdates decompression and penetrative deformation during the HP/HT–MT–LT transition (Fig. 14). The geodynamic context of decompression and deformation is lithospheric thinning. Beneath the Marsabit area, this was related to either the formation of the Anza Graben and/or initial EARS-related rifting (HP/HT–MT–LT transition). Absolute time constraints for the age of the HP/HT–MT transition are difficult to obtain. Estimating the maximum age of the HP/HT–MT transition by diffusion modelling using published diffusion coefficients for REE (van Orman *et al.*, 2001) and Al in clinopyroxene (Sautter *et al.*, 1988) gave unsatisfactory results. The smallest cpx-I grain analysed that still shows HREE zoning has a diameter of 0·6 mm. Assuming a constant temperature of 900°C, after decompression and cooling to the MT stage, it would take a maximum of 20–170 Myr to completely re-equilibrate the Yb contents in such a grain. However, the xenoliths further cooled to much lower temperatures than 900°C, which would result in considerably longer re-equilibration times (e.g. a time span of ~3 Gyr at 800°C). Similarly, calculating the duration of the decompression event using the Al zoning patterns in clinopyroxene (Al increase from core to rim; e.g. Fig. 12b) would yield time spans of the order of 10^5–10^6 years at 1000°C, ~10^7 years at 900°C, and 10^8–10^9 years at 800°C, respectively. Therefore, as the time spans between Mesozoic and Tertiary rifting are relatively short (or even overlapping; Reeves *et al.*, 1987), diffusion modelling is unlikely to better constrain the timing of decompression observed in mantle xenoliths from Marsabit.

However, comparison with geological and geophysical data shows that lithospheric thinning in the course of Mesozoic rifting would be in good agreement with several conclusions from other studies. Cooling, relatively cold deformation, and the lack of metasomatism associated with decompression would be consistent with the generally volcanic-poor nature of the whole Mesozoic Central African Rift System (including the Anza Graben; e.g. Reeves *et al.*, 1987; Morley, 1999, and references therein). Further, it would be consistent with the picture of the present-day structures beneath the Kenya rift. Anomalously low-velocity material is confined to the surface expression of the present-day rift (Mechie *et al.*, 1997, and references therein). This argues in favour of a model where the lithospheric mantle deforms by pure shear beneath the rift axis, and against models where lithospheric thinning is offset beneath the rift flanks, e.g. below Marsabit (Mechie *et al.*, 1997).

Additional arguments in favour of lithospheric thinning in the context of Mesozoic rifting come from other xenolith localities. Although porphyroclastic peridotites also occur beneath Mega (Bedini *et al.*, 1997), they do not show the intense decompression- and deformation-related features revealed by the samples from Marsabit. This means that the lithospheric mantle beneath Mega probably only experienced EARS-related modifications, consistent with the geographical position of Mega at the border of the Afar dome, away from the Anza Graben (Fig. 1a). Xenolith localities further to the south, far from the Anza Graben, in southern Kenya and Tanzania, reflect a still thick lithospheric mantle (Fig. 12b), but one variably metasomatized by EARS-related melts or fluids (e.g. Dawson & Smith, 1988; Henjes-Kunst & Altherr, 1992; Rudnick *et al.*, 1993; Chesley *et al.*, 1999; Lee & Rudnick, 1999; Dawson, 2002). In contrast, xenoliths

from Marsabit, situated above the Anza Graben, record Mesozoic rifting processes in addition to EARS-related metasomatism.

The penetrative deformation during the HT/HP–MT transition resulted in considerable small-scale heterogeneities comprising variously depleted peridotite mingled with originally mafic lithologies (grt-pyroxenite). The heated mantle parts (represented by Group II xenoliths), interpreted to have interacted with melts parental to the Marsabit Quaternary magmas, also show evidence for such heterogeneities. Percolation through, or assimilation of such heterogeneous material may account for the heterogeneous nature of the magmas of this region (Marsabit: Volker, 1990; Huri Hills: Class *et al.*, 1994; see Fig. 1b), as reflected by the trace element and isotope signatures of the lavas. However, the compositional features observed in the Group II xenoliths do not allow us to conclude whether the melts responsible for metasomatism contain a mantle-plume signature or not. Finally, in the mantle lithosphere beneath Marsabit, the thermal conditions prior to decompression and deformation (i.e. the HP/HT stage) were similar to the present-day situation observed in xenoliths from southern Kenya, beneath the Chyulu Hills (Fig. 12b; Henjes-Kunst & Altherr, 1992; Altherr *et al.*, in preparation), which is consistent with the conclusions of Henjes-Kunst & Altherr (1992).

ACKNOWLEDGEMENTS

Many thanks go to Othmar Müntener. Numerous discussions contributed to the substance of this study. Thanks go also to Edwin Gnos (Bern) and Hans-Peter Meyer (Heidelberg) for assistance with microprobe work. We are grateful to Tanya Furman, Else-Ragnhild Neumann, Elisabetta Rampone and Yigang Xu for thorough and constructive reviews, which greatly improved the quality of this paper, and to Marjorie Wilson for valuable comments and editorial handling. This work is part of a grant from the Swiss National Science Foundation (No. 200021-100647/1) to A.K.

SUPPLEMENTARY DATA

Supplementary data for this paper are available at *Journal of Petrology* online.

REFERENCES

Achauer, U. & KRISP Teleseismic Working Group (1994). New ideas on the Kenya rift based on the inversion of the combined dataset of the 1985 and 1989/90 seismic tomography experiments. *Tectonophysics* **236**, 305–329.

Baker, B. H. (1987). Outline of the petrology of the Kenya rift alkaline province. In: Fitton, J. G. & Upton, B. G. J. (eds) *Alkaline Igneous Rocks. Geological Society, London, Special Publications* **30**, 293–311.

Ballhaus, C., Berry, R. F. & Green, D. H. (1991). High pressure experimental calibration of the olivine–orthopyroxene–spinel oxygen geobarometer: implications for the oxidation state of the upper mantle. *Contributions to Mineralogy and Petrology* **107**, 27–40.

Bedini, R. M. & Bodinier, J.-L. (1999). Distribution of incompatible trace elements between the constituents of spinel peridotite xenoliths: ICP-MS data from the East African Rift. *Geochimica et Cosmochimica Acta* **63**, 3883–3900.

Bedini, R. M., Bodinier, J.-L., Dautria, J.-M. & Morten, L. (1997). Evolution of LILE-enriched small melt fractions in the lithospheric mantle: a case study from the East African Rift. *Earth and Planetary Science Letters* **153**, 67–83.

Bodinier, J. L., Dupuy, C. & Dostal, J. (1988). Geochemistry and petrogenesis of eastern Pyrenean peridotites. *Geochimica et Cosmochimica Acta* **52**, 2893–2907.

Bodinier, J. L., Vasseur, G., Vernières, J., Dupuy, C. & Fabriès, J. (1990). Mechanisms of mantle metasomatism—geochemical evidence from the Lherz orogenic peridotite. *Journal of Petrology* **31**, 597–628.

Bodinier, J.-L., Menzies, M. A., Shimizu, N., Frey, F. A. & McPherson, E. (2004). Silicate, hydrous and carbonate metasomatism at Lherz, France: contemporaneous derivates of silicate melt–harzburgite reaction. *Journal of Petrology* **45**, 299–320.

Bosworth, W. & Morley, C. K. (1994). Structural and stratigraphic evolution of the Anza rift, Kenya. *Tectonophysics* **236**, 93–115.

Brey, G. P. & Köhler, T. (1990). Geothermobarometry in four-phase lherzolites II. New thermobarometers, and practical assessment of existing thermobarometers. *Journal of Petrology* **31**, 1353–1378.

Brey, G. P., Köhler, T. & Nickel, K. G. (1990). Geothermobarometry in four-phase lherzolites I. Experimental results from 10 to 60 kb. *Journal of Petrology* **31**, 1313–1352.

Brotzu, P., Morbideli, L., Nicoletti, M., Piccirillo, E. M. & Traversa, G. (1984). Miocene to Quaternary volcanism in eastern Africa: sequence and chronology. *Tectonophysics* **101**, 75–86.

Carroll Webb, S. A. & Wood, B. J. (1986). Spinel–pyroxene–garnet relationship and their dependence on Cr/Al ratio. *Contributions to Mineralogy and Petrology* **92**, 471–480.

Chakraborty, S., Farver, J. R., Yund, R. A. & Rubie, D. C. (1994). Mg tracer diffusion in synthetic forsterite and San Carlos olivine as a function of P, T and fO_2. *Physics and Chemistry of Minerals* **21**, 489–500.

Chesley, J. T., Rudnick, R. L. & Lee, C. T. (1999). Re–Os systematics of mantle xenoliths from the East African Rift: age, structure, and history of the Tanzanian craton. *Geochimica et Cosmochimica Acta* **63**, 1203–1217.

Class, C., Altherr, R., Volker, F., Eberz, G. & McCulloch, M. T. (1994). Geochemistry of Pliocene to Quaternary alkali basalts from the Hurri Hills, northern Kenya. *Chemical Geology* **113**, 1–22.

Cohen, R. S., O'Nions, R. K. & Dawson, J. B. (1984). Isotope geochemistry of xenoliths from East Africa—implications for development of mantle reservoirs and their interaction. *Earth and Planetary Science Letters* **68**, 209–220.

Conticelli, S., Sintoni, M. F., Abebe, T., Mazzarini, F. & Manetti, P. (1999). Petrology and geochemistry of ultramafic xenoliths and host lavas from the Ethiopian volcanic province: an insight into the upper mantle under eastern Africa. *Acta Vulcanologica* **11**, 143–159.

Dawson, J. B. (2002). Metasomatism and partial melting in upper-mantle peridotite xenoliths from the Lashaine volcano, Northern Tanzania. *Journal of Petrology* **43**, 1749–1777.

Dawson, J. B. & Smith, J. V. (1988). Metasomatized and veined upper-mantle xenoliths from Pello Hill, Tanzania—evidence for anomalously-light mantle beneath the Tanzanian sector of the East African Rift valley. *Contributions to Mineralogy and Petrology* **100**, 510–527.

Dawson, J. B., Powell, D. G. & Reid, A. M. (1970). Ultrabasic xenoliths and lava from the Lashaine Volcano, northern Tanzania. *Journal of Petrology* **11**, 519–548.

Debayle, E., Leveque, J. J. & Cara, M. (2001). Seismic evidence for a deeply rooted low-velocity anomaly in the upper mantle beneath the northeastern Afro/Arabian continent. *Earth and Planetary Science Letters* **193**, 423–436.

Delaney, J. S., Smith, J. V., Carswell, D. A. & Dawson, J. B. (1980). Chemistry of micas from kimberlites and xenoliths—II. Primary- and secondary-textured micas from peridotite xenoliths. *Geochimica et Cosmochimica Acta* **44**, 857–872.

Dick, H. J. B. & Bullen, T. (1984). Chromian spinel as a petrogenetic indicator in abyssal and alpine-type peridotites and spatially associated lavas. *Contributions to Mineralogy and Petrology* **86**, 54–76.

Ebinger, C. J. & Ibrahim, A. (1994). Multiple episodes of rifting in Central and East Africa—a reevaluation of gravity data. *Geologische Rundschau* **83**, 689–702.

Ebinger, C. J. & Sleep, N. H. (1998). Cenozoic magmatism throughout east Africa resulting from impact of a single plume. *Nature* **395**, 788–791.

Eggins, S. M., Rudnick, R. L. & McDonough, W. F. (1998). The composition of peridotites and their minerals: a laser-ablation ICP-MS study. *Earth and Planetary Science Letters* **154**, 53–71.

Fuchs, K., Altherr, R., Müller, B. & Prodehl, C. (1997). Structure and dynamic processes in the lithosphere of the Afro-Arabian rift system. *Tectonophysics (special issue)* **278**, 352 pp.

Furman, T., Bryce, J. G., Karson, J. & Iotti, A. (2004). East African rift system (EARS) plume structure: insights from Quaternary mafic lavas of Turkana, Kenya. *Journal of Petrology* **45**, 1069–1088.

Gasparik, T. (1987). Orthopyroxene thermobarometry in simple and complex systems. *Contributions to Mineralogy and Petrology* **96**, 357–370.

George, R., Rogers, N. & Kelley, S. (1998). Earliest magmatism in Ethiopia: evidence for two mantle plumes in one flood basalt province. *Geology* **26**, 923–926.

George, R. M. & Rogers, N. W. (2002). Plume dynamics beneath the African plate inferred from the geochemistry of the Tertiary basalts of southern Ethiopia. *Contributions to Mineralogy and Petrology* **144**, 286–304.

Glaser, S. M., Foley, S. F. & Günther, D. (1999). Trace element compositions of minerals in garnet and spinel peridotite xenoliths from the Vitim volcanic field, Transbaikalia, eastern Siberia. *Lithos* **48**, 263–285.

Greene, L. C., Richards, D. R. & Johnson, R. A. (1991). Crustal structure and tectonic evolution of the Anza rift, northern Kenya. *Tectonophysics* **197**, 203–211.

Günther, D., Frischknecht, R., Heinrich, C. A. & Kahlert, H. J. (1997). Capabilities of an argon fluoride 193 nm excimer laser for laser ablation inductively coupled plasma mass spectrometry micro-analysis of geological materials. *Journal of Analytical Atomic Spectrometry* **12**, 939–944.

Heinrich, C. A., Pettke, T., Halter, W. E., Aigner-Torres, M., Audetat, A., Gunther, D., Hattendorf, B., Bleiner, D., Guillong, M. & Horn, I. (2003). Quantitative multi-element analysis of minerals, fluid and melt inclusions by laser-ablation inductively-coupled-plasma mass-spectrometry. *Geochimica et Cosmochimica Acta* **67**, 3473–3497.

Henjes-Kunst, F. & Altherr, R. (1992). Metamorphic petrology of xenoliths from Kenya and northern Tanzania and implications for geotherms and lithospheric structures. *Journal of Petrology* **33**, 1125–1156.

Ionov, D. A. (2004). Chemical variations in peridotite xenoliths from Vitim, Siberia: inferences for REE and Hf behaviour in the garnet-facies upper mantle. *Journal of Petrology* **45**, 343–367.

Ionov, D. A., Griffin, W. L. & O'Reilly, S. Y. (1997). Volatile-bearing minerals and lithophile trace elements in the upper mantle. *Chemical Geology* **141**, 153–184.

Ionov, D. A., Bodinier, J.-L., Mukasa, S. B. & Zanetti, A. (2002). Mechanisms and sources of mantle metasomatism: major and trace element compositions of peridotite xenoliths from Spitsbergen in the context of numerical modelling. *Journal of Petrology* **43**, 2219–2259.

Jones, A. P., Smith, J. V. & Dawson, J. B. (1983). Glasses in mantle xenoliths from Olmani, Tanzania. *Journal of Geology* **91**, 167–178.

Kabeto, K., Sawada, Y., Iizumi, S. & Wakatsuki, T. (2001). Mantle sources and magma–crust interactions in volcanic rocks from the northern Kenya rift: geochemical evidence. *Lithos* **56**, 111–139.

Key, R. M., Rop, B. P. & Rundle, C. C. (1987). The development of the late Cenozoic alkali basaltic Marsabit shield volcano, northern Kenya. *Journal of African Earth Sciences* **6**, 475–491.

Key, R. M., Charsley, T. J., Hackman, B. D., Wilkinson, A. F. & Rundle, C. C. (1989). Superimposed upper Proterozoic collision-controlled orogenies in the Mozambique orogenic belt of Kenya. *Precambrian Research* **44**, 197–225.

King, S. D. & Ritsema, J. (2000). African hot spot volcanism: small-scale convection in the upper mantle beneath cratons. *Science* **290**, 1137–1140.

Kornprobst, J. (1966). A propos des péridotites du massif des Beni-Bouchera (Rif Septentrional Maroc). *Bulletin de la Société Française de Minéralogie et de Cristallographie* **89**, 399–404.

Lee, C.-T. & Rudnick, R. (1999). Compositionally stratified cratonic lithosphere; petrology and geochemistry of peridotite xenoliths from the Labait Volcano, Tanzanie. In: Gurney, J., Gurney, J. L., Pascoe, M. D. & Richardson, S. H. (eds) *Proceedings of the 7th International Kimberlite Conference*. Cape Town: Red Roof Design, pp. 503–521.

Lorand, J. P., Reisberg, L. & Bedini, R. M. (2003). Platinum-group elements and melt percolation processes in Sidamo spinel peridotite xenoliths, Ethiopia, East African Rift. *Chemical Geology* **196**, 57–75.

MacDonald, R., Rogers, N. W., Fitton, J. G., Black, S. & Smith, M. (2001). Plume–lithosphere interactions in the generation of the basalts of the Kenya Rift, East Africa. *Journal of Petrology* **42**, 877–900.

McDonough, W. F. & Sun, S. S. (1995). The composition of the Earth. *Chemical Geology* **120**, 223–253.

McKenzie, D. & Bickle, M. J. (1988). The volume and composition of melt generated by extension of the lithosphere. *Journal of Petrology* **29**, 625–679.

Mechie, J., Keller, G. R., Prodehl, C., Khan, M. A. & Gaciri, S. J. (1997). A model for the structure, composition and evolution of the Kenya rift. *Tectonophysics* **278**, 95–119.

Meert, J. G. (2003). A synopsis of events related to the assembly of eastern Gondwana. *Tectonophysics* **362**, 1–40.

Menzies, M., Kempton, P. & Dungan, M. (1985). Interaction of continental lithosphere and asthenospheric melts below the Geronimo volcanic field, Arizona, USA. *Journal of Petrology* **26**, 663–693.

Morishita, T. & Arai, S. (2003). Evolution of spinel–pyroxene symplectite in spinel-lherzolites from the Horoman complex, Japan. *Contributions to Mineralogy and Petrology* **144**, 509–522.

Morley, C. K. (1999). Tectonic evolution of the East African Rift System and the modifying influence of magmatism: a review. *Acta Vulcanologica* **11**, 1–19.

Müntener, O. & Hermann, J. (1996). The Val Malenco lower crust–upper mantle complex and its field relations (Italian Alps). *Schweizerische Mineralogische und Petrographische Mitteilungen* **76**, 475–500.

Navon, O. & Stolper, E. (1987). Geochemical consequences of melt percolation: the upper mantle as a chromatographic column. *Journal of Geology* **95**, 285–308.

Niida, K. & Green, D. H. (1999). Stability and chemical composition of pargasitic amphibole in MORB pyrolite under upper mantle conditions. *Contributions to Mineralogy and Petrology* **135**, 18–40.

Nyblade, A. A. & Brazier, R. A. (2002). Precambrian lithospheric controls on the development of the East African rift system. *Geology* **30**, 755–758.

Nyblade, A. A., Owens, T. J., Gurrola, H., Ritsema, J. & Langston, C. A. (2000). Seismic evidence for a deep upper mantle thermal anomaly beneath east Africa. *Geology* **28**, 599–602.

Olker, B. (2001). Entwicklung und Anwendung eines Computerprogrammes zur numerischen Modellierung von Diffusionsprofilen in Mineralkörnern. Ph.D. thesis, University of Heidelberg, 269 pp.

Pearson, D. G., Canil, D. & Shirey, S. B. (2003). Mantle samples included in volcanic rocks: xenoliths and diamonds. In: Carlson, R. W. (ed.) *Treatise on Geochemistry*. Amsterdam: Elsevier, pp. 171–275.

Pettke, T., Halter, W. E., Webster, J. D., Aigner-Torres, M. & Heinrich, C. A. (2004). Accurate quantification of melt inclusion chemistry by LA-ICPMS: a comparison with EMP and SIMS and advantages and possible limitations of these methods. *Lithos* **78**, 333–361.

Pike, J. E. N., Meyer, C. E. & Wilshire, H. G. (1980). Petrography and chemical composition of a suite of ultramafic xenoliths from Lashaine, Tanzania. *Journal of Geology* **88**, 343–352.

Pollack, H. N. & Chapman, D. S. (1977). Regional variation of heat-flow, geotherms, and lithospheric thickness. *Tectonophysics* **38**, 279–296.

Prodehl, C., Keller, G. R. & Khan, M. A. (1994). Crustal and upper mantle structure of the Kenya rift. *Tectonophysics (special publication)* **236**, 483 pp.

Rampone, E., Bottazzi, P. & Ottolini, L. (1991). Complementary Ti and Zr anomalies in orthopyroxene and clinopyroxene from mantle peridotites. *Nature* **354**, 518–520.

Reeves, C. V., Karanja, F. M. & MacLeod, I. N. (1987). Geophysical evidence for a failed Jurassic rift and triple junction in Kenya. *Earth and Planetary Science Letters* **81**, 299–311.

Reid, A. M. & Dawson, J. B. (1972). Olivine–garnet reaction in peridotites from Tanzania. *Lithos* **5**, 115–124.

Reisberg, L., Lorand, J. P. & Bedini, R. M. (2004). Reliability of Os model ages in pervasively metasomatized continental mantle lithosphere: a case study of Sidamo spinel peridotite xenoliths (East African Rift, Ethiopia). *Chemical Geology* **208**, 119–140.

Rogers, N., MacDonald, R., Fitton, J. G., George, R., Smith, M. & Barreiro, B. (2000). Two mantle plumes beneath the East African rift system: Sr, Nd and Pb isotope evidence from Kenya rift basalts. *Earth and Planetary Science Letters* **176**, 387–400.

Rooney, T. O., Furman, T., Yirgu, G. & Ayalew, D. (2005). Structure of the Ethiopian lithosphere: xenolith evidence in the Main Ethiopian Rift. *Geochimica et Cosmochimica Acta* **69**, 3889–3910.

Rudnick, R. L., McDonough, W. F. & Chappell, B. W. (1993). Carbonatite metasomatism in the northern Tanzanian mantle: petrographic and geochemical characteristics. *Earth and Planetary Science Letters* **114**, 463–475.

Sachtleben, T. & Seck, H. A. (1981). Chemical control of Al-solubility in orthopyroxene and its implications on pyroxene geothermometry. *Contributions to Mineralogy and Petrology* **78**, 157–165.

Sautter, V., Jaoul, O. & Abel, F. (1988). Aluminum diffusion in diopside using the $^{27}Al(p,\gamma)^{28}Si$ nuclear reaction: preliminary results. *Earth and Planetary Science Letters* **23**, 109–114.

Schubert, W. (1977). Reactions in Alpine type peridotite of Ronda (Spain) and in its partial fusion products. *Contributions to Mineralogy and Petrology* **62**, 205–220.

Seitz, H.-M., Altherr, R. & Ludwig, T. (1999). Partitioning of transition elements between orthopyroxene and clinopyroxene in peridotitic and websteritic xenoliths: new empirical geothermometers. *Geochimica et Cosmochimica Acta* **63**, 3967–3982.

Shackleton, R. M. (1993). Tectonics of the Mozambique Belt in East Africa. In: Prichard, H. M., Alabaster, T., Harris, N. B. & Neary, C. R. (eds) *Magmatic Processes and Plate Tectonics. Geological Society, London, Special Publications* **76**, 345–362.

Simon, N. S. C., Irvine, G. J., Davies, G. R., Pearson, D. G. & Carlson, R. W. (2003). The origin of garnet and clinopyroxene in 'depleted' Kaapvaal peridotites. *Lithos* **71**, 289–322.

Skulski, T., Minarik, W. & Watson, E. B. (1994). High-pressure experimental trace-element partitioning between clinopyroxene and melt. *Chemical Geology* **117**, 127–147.

Smith, D. (1999). Temperatures and pressures of mineral equilibration in peridotite xenoliths: review, discussion, and implications. In: Fei, Y., Bertka, C. M. & Mysen, B. O. (eds) *Mantle Petrology: Field Observation and High-Pressure Experimentation. A Tribute to Francis R. (Joe) Boyd. Geochemical Society, Special Publications* **6**, 171–188.

Späth, A., le Roex, A. P. & Opiyo-Akech, N. (2001). Plume–lithosphere interaction and the origin of continental rift-related alkaline volcanism—the Chyulu Hills volcanic province, southern Kenya. *Journal of Petrology* **42**, 765–787.

Stern, R. J. (1994). Arc assembly and continental collision in the Neoproterozoic East African orogen—implications for the consolidation of Gondwanaland. *Annual Review of Earth and Planetary Sciences* **22**, 319–351.

Stewart, K. & Rogers, N. (1996). Mantle plume and lithosphere contributions to basalts from southern Ethiopia. *Earth and Planetary Science Letters* **139**, 195–211.

Suwa, K., Yusa, Y. & Kishida, N. (1975). Petrology of peridotite nodules from Ndonyuo Olnchoro, Samburu district central Kenya. *Physics and Chemistry of the Earth* **9**, 273–286.

Tabit, A., Kornprobst, J. & Woodland, A. B. (1997). The garnet peridotites of the Beni Bousera massif (Morocco): tectonic mixing and iron–magnesium interdiffusion. *Comptes Rendus de l'Academie des Sciences* **325**, 665–670.

Takazawa, E., Frey, F., Shimizu, N. & Obata, M. (1996). Evolution of the Horoman Peridotite (Hokkaido, Japan): implications from pyroxene compositions. *Chemical Geology* **134**, 3–26.

Taylor, W. R. (1998). An experimental test of some geothermometer and geobarometer formulations for upper mantle peridotites with applications to the thermobarometry of fertile lherzolites and garnet websterites. *Neues Jahrbuch für Mineralogie, Abhandlungen* **172**, 381–408.

Ulianov, A. & Kalt, A. (2006). Mg–Al sapphirine- and Ca–Al hibonite-bearing granulite xenoliths from the Chyulu Hills Volcanic Field, Kenya. *Journal of Petrology* **47**, 901–927.

Vannucci, R., Shimizu, N., Piccardo, G. B., Ottolini, L. & Bottazzi, P. (1993). Distribution of trace elements during breakdown of mantle garnet: an example from Zabargad. *Contributions to Mineralogy and Petrology* **113**, 437–449.

Vannucci, R., Piccardo, G. B., Rivalenti, G., Zanetti, A., Rampone, E., Ottolini, L., Oberti, R., Mazzucchelli, M. & Bottazzi, P. (1995). Origin of LREE-depleted amphiboles in the subcontinental mantle. *Geochimica et Cosmochimica Acta* **59**, 1763–1771.

Van der Wal, D. & Vissers, R. L. M. (1996). Structural petrology of the Ronda peridotite, SW Spain: deformation history. *Journal of Petrology* **37**, 23–43.

Van Orman, J. A., Grove, T. L. & Shimizu, N. (2001). Rare earth element diffusion in diopside: influence of temperature, pressure, and ionic radius, and an elastic model for diffusion in silicates. *Contributions to Mineralogy and Petrology* **141**, 687–703.

Vasseur, G., Vernières, J. & Bodinier, J.-L. (1991). Modelling of trace element transfer between mantle melt and heterogranular peridotite matrix. *Journal of Petrology, Special Lherzolites Issue*, 41–54.

Vauchez, A., Dineur, F. & Rudnick, R. (2005). Microstructure, texture and seismic anisotropy of the lithospheric mantle above a mantle plume: insights from the Labait volcano xenoliths (Tanzania). *Earth and Planetary Science Letters* **232**, 295–314.

Vernières, J., Godard, M. & Bodinier, J.-L. (1997). A plate model for the simulation of trace element fractionation during partial melting and magma transport in the Earth's upper mantle. *Journal of Geophysical Research* **102**, 24771–24784.

Volker, F. (1990). Geochemie der quartären Vulkanite auf der Ostschulter des Kenia-Rifts. Ph.D. thesis, University of Karlsruhe, 204 pp.

Wallace, R. C. (1975). Mineralogy and petrology of xenoliths in a diatreme from South Westland, New Zealand. *Contributions to Mineralogy and Petrology* **49**, 191–199.

Weeraratne, D. S., Forsyth, D. W., Fischer, K. M. & Nyblade, A. A. (2003). Evidence for an upper mantle plume beneath the Tanzanian craton from Rayleigh wave tomography. *Journal of Geophysical Research* **108**, 2427, doi: 10.1029/2002JB002273.

Werling, F. & Altherr, R. (1997). Thermal evolution of the lithosphere beneath the French Massif Central as deduced from geothermobarometry on mantle xenoliths. *Tectonophysics* **275**, 119–141.

Winn, R. D., Steinmetz, J. C. & Kerekgyarto, W. L. (1993). Stratigraphy and rifting history of the Mesozoic–Cenozoic Anza rift, Kenya. *AAPG Bulletin* **77**, 1989–2005.

Witt-Eickschen, G. & O'Neill, H. St. C. (2005). The effect of temperature on the equilibrium distribution of trace elements between clinopyroxene, orthopyroxene, olivine and spinel in upper mantle peridotite. *Chemical Geology* **221**, 65–101.

Witt-Eickschen, G. & Seck, H. A. (1991). Solubility of Ca and Al in orthopyroxene from spinel peridotite: an improved version of an empirical geothermometer. *Contributions to Mineralogy and Petrology* **106**, 431–439.

Wood, B. J., Blundy, J. D. & Robinson, J. A. C. (1999). The role of clinopyroxene in generating U-series disequilibrium during mantle melting. *Geochimica et Cosmochimica Acta* **63**, 1613–1620.

Xu, Y. & Bodinier, J.-L. (2004). Contrasting enrichments in high- and low-temperature mantle xenoliths from Nushan, eastern China: results of a single metasomatic event during lithospheric accretion? *Journal of Petrology* **45**, 321–341.

Xu, Y. G., Menzies, M. A., Bodinier, J. L., Bedini, R. M., Vroon, P. & Mercier, J. C. C. (1998). Melt percolation and reaction atop a plume: evidence from the poikiloblastic peridotite xenoliths from Boree (Massif Central, France). *Contributions to Mineralogy and Petrology* **132**, 65–84.

Yu, J. H., O'Reilly, S. Y., Zhang, M., Griffin, W. L. & Xu, X. S. (2006). Roles of melting and metasomatism in the formation of the lithospheric mantle beneath the Leizhou Peninsula, South China. *Journal of Petrology* **47**, 355–383.